7-2015

A Meteorological Analysis of the 2013 Alberta Flood: Antecendent Large-Scale Flow Pattern and Synoptic-Dynamic Characteristics

Shawn M. Milrad
Embry-Riddle Aeronautical University, milrads@erau.edu

John R. Gyakum
McGill University

Eyad H. Atallah
McGill University

Scholarly Commons Citation

Milrad, S. M., Gyakum, J. R., & Atallah, E. H. (2015). A Meteorological Analysis of the 2013 Alberta Flood: Antecendent Large-Scale Flow Pattern and Synoptic-Dynamic Characteristics. *Monthly Weather Review, 143*(7). https://doi.org/10.1175/MWR-D-14-00236.1

A Meteorological Analysis of the 2013 Alberta Flood: Antecedent Large-Scale Flow Pattern and Synoptic–Dynamic Characteristics

SHAWN M. MILRAD

Department of Applied Aviation Sciences, Embry-Riddle Aeronautical University, Daytona Beach, Florida

JOHN R. GYAKUM AND EYAD H. ATALLAH

Department of Atmospheric and Oceanic Sciences, McGill University, Montreal, Quebec, Canada

(Manuscript received 20 July 2014, in final form 31 March 2015)

ABSTRACT

The 19–21 June 2013 Alberta flood was the costliest (CAD $6 billion) natural disaster in Canadian history. The flood was caused by a combination of above-normal spring snowmelt in the Canadian Rockies, large antecedent precipitation, and an extreme rainfall event on 19–21 June that produced rainfall totals of 76 mm in Calgary and 91 mm in the foothills. As is typical of flash floods along the Front Range of the Rocky Mountains, rapidly rising streamflow proceeded to move downhill (eastward) into Calgary.

A meteorological analysis traces an antecedent Rossby wave train across the North Pacific Ocean, starting with intense baroclinic development over East Asia on 11 June. Subsequently, downstream Rossby wave development occurred across the North Pacific; a 1032-hPa subtropical anticyclone located northeast of Hawaii initiated a southerly atmospheric river into Alaska, which contributed to the development of a cutoff anticyclone over Alaska and a Rex block (ridge to the north, cyclone to the south) in the northeastern North Pacific. Upon breakdown of the Rex block, lee cyclogenesis occurred in Montana and strong easterly upslope flow was initiated in southern Alberta.

The extreme rainfall event was produced in association with a combination of quasigeostrophically and orographically forced ascent, which acted to release conditional and convective instability. As in past Front Range flash floods, moisture flux convergence and positive θ_e advection were collocated with the heavy rainfall. Backward trajectories show that air parcels originated in the northern U.S. plains, suggesting that evapotranspiration from the local land surface may have acted as a moisture source.

1. Introduction

Flash flooding is the largest cause of North American fatalities associated with convection (e.g., Doswell et al. 1996) and is often the most costly (e.g., Schumacher and Johnson 2005). The flooding that struck Calgary, Alberta, and the surrounding southern Alberta foothills on 19–21 June 2013 was the costliest natural disaster in Canadian history (Environment Canada 2014b), surpassing the 1998 ice storm in eastern Canada (e.g., Gyakum and Roebber 2001) and the 1996 Saguenay, Quebec, flood (Milbrandt and Yau 2001). There were four deaths, thousands of Albertans were left homeless, and total damage losses were estimated at 2013-adjusted CAD $5–$6 billion (Environment Canada 2014b; Government of Alberta 2014). Severe flood damage was widespread in both Calgary and the foothills to the west (Fig. 1). A complete evacuation of downtown Calgary was necessary on 20 and 21 June, and famous sites, such as the professional hockey arena (Scotiabank Saddledome) and the Calgary Stampede, were heavily damaged (Huffington Post Alberta 2014).

The Alberta flood was caused in part by unusual meteorological and hydrological precursor events, including large spring snowmelt in the foothills of the Canadian Rockies and heavy antecedent precipitation in May and early June. The tipping point was an extreme rainfall event on 19–21 June (Environment Canada 2014b), which we investigate here. Streamflow in the Elbow and Bow Rivers increased dramatically, allowing damaging flood waters in the foothills (Fig. 1a) to then flow downhill

Corresponding author address: Shawn M. Milrad, Department of Applied Aviation Sciences, Embry-Riddle Aeronautical University, 600 S. Clyde Morris Blvd., Daytona Beach, FL 32114.
E-mail: shawn.milrad@gmail.com

DOI: 10.1175/MWR-D-14-00236.1

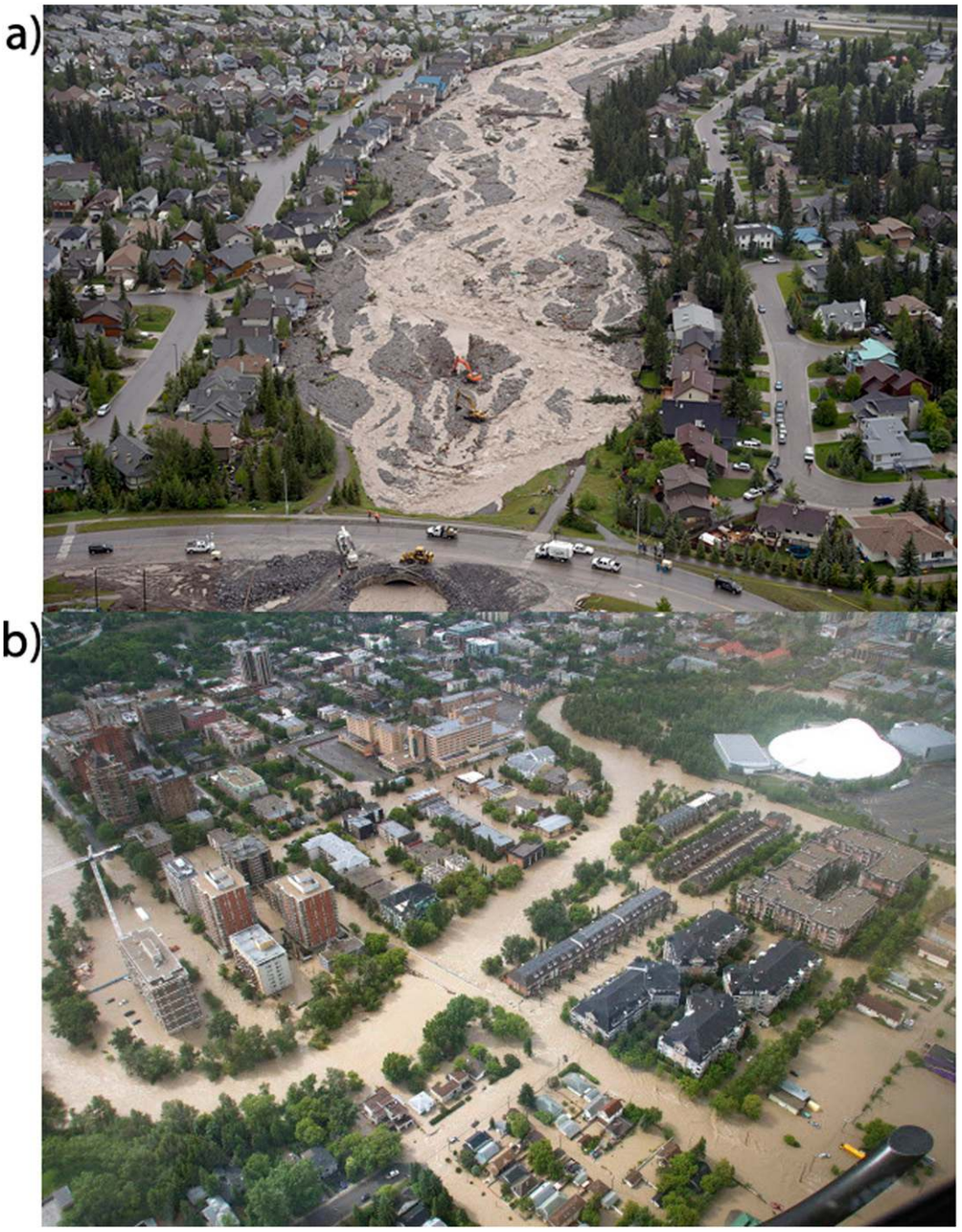

FIG. 1. Flood photos from 21 Jun 2013 of (a) Canmore (140 km west-northwest of Calgary; Huffington Post Alberta 2014) and (b) downtown Calgary (Calgary Herald 2014).

(downstream) into downtown Calgary (Fig. 1b). Both model and human quantitative precipitation forecasts did predict a wet period for much of southern Alberta, but as is typical in most extreme rainfall events (e.g., Lavers and Villarini 2013; Hamill 2014; Gochis et al. 2015), forecasts underestimated the magnitude of the heaviest precipitation.

Past research on warm-season flash floods includes Maddox et al. (1978, 1979, 1980), Caracena et al. (1979), and Schumacher and Johnson (2005, 2006, 2008, 2009). These sets of work largely pertained to flash flood events in the United States caused by mesoscale convective systems (MCSs), including in the Rockies' Front Range. Research on high-impact precipitation events in Canada

has been relatively limited, although Milbrandt and Yau (2001) performed mesoscale model simulations for the 1996 Saguenay flood, and Szeto et al. (2011) detailed the synoptic characteristics of a drought-breaking rainfall event in the Canadian prairies in June 2002. Brimelow and Reuter (2005) examined three extreme rainfall events over northwestern Canada and noted air parcel trajectories and moisture transport directly from the Gulf of Mexico, with air forced upward primarily by the orography in western Canada. Flesch and Reuter (2012) performed high-resolution model simulations on two flooding events in southern Alberta and found that a simple "terrain reduction" scheme reduced precipitation in the foothills by 50%–75%.

Two recent high-impact flash flood events in North America were (i) the May 2010 Nashville, Tennessee, flood, and (ii) the Great Colorado flood of September 2013. For the Nashville event, Moore et al. (2012) traced air parcels back to the equator, with a plume of large integrated water vapor (IWV) extending northward into the southeastern United States. Moore et al. (2012) found that two successive quasi-stationary MCSs moved over the region, with training and back-building convective echoes forming along a slow-moving cold front (e.g., Maddox et al. 1978; Schumacher and Johnson 2005). Moore et al. (2012) also noted a strong pressure gradient between an upstream cyclone and a downstream anticyclone, which helped to enhance the southerly atmospheric river (AR) of IWV. Lynch and Schumacher (2014) used ensemble modeling techniques to show that the intensity and duration of the AR was sensitive to small changes in the intensity of the upstream cyclone; counterintuitively, heavier precipitation was found in ensemble members with a weaker upstream cyclone because it allowed a narrower, more focused low-level jet. On a climatological basis, Dirmeyer and Kinter (2010) observed a stronger Great Plains low-level jet when the intensity of the downstream subtropical ridge was above normal, and Newman et al. (2012) found narrower ARs were associated with stronger downstream subtropical anticyclones.

In the 2013 Great Colorado flood, up to 450 mm of rainfall were recorded in Boulder County (Gochis et al. 2015). Flooding was widespread and resulted in more than $2 billion (U.S. dollars) in damage (Gochis et al. 2015). Lavers and Villarini (2013) found that the return period of the total accumulated precipitation during the Colorado flood was a few hundred years. As in the Alberta flood, the rainfall was not particularly associated with strong or severe thunderstorms, but it was characterized by several episodes of long-duration moderate to heavy precipitation. The synoptic-scale patterns were also similar in that both featured very stagnant upper-tropospheric flow and strong southerly moisture transport on the western periphery of a subtropical anticyclone (Gochis et al. 2015). While most deterministic and ensemble prediction systems did forecast a wet period for the affected areas (Lavers and Villarini 2013; Hamill 2014; Gochis et al. 2015), they again massively underforecasted the magnitude of the event. Moreover, both the Colorado and Alberta floods were caused by a combination of meteorological, hydrological, and orographic processes; that is, while the meteorological setup produced heavy rainfall, certain precursor hydrological factors (increased snowmelt, above-normal soil moisture, etc.) contributed to the magnitude of the flooding. In both cases, the heaviest rainfall fell in the foothills (at higher elevations), allowing for markedly increased streamflow to move downhill (downstream) toward more populated areas, such as Boulder (Gochis et al. 2015) and Calgary (Fig. 1).

TABLE 1. For 19–21 Jun 2013, daily and event precipitation totals (mm) at the Calgary International Airport (elevation: 1084 m) and Banff (elevation: 1397 m), from the EC historical climate database. Note that the date refers to midnight–midnight local time (MDT), which is 0600–0600 UTC.

Time period	Calgary International Airport	Banff
19 Jun	7.8	17.1
20 Jun	45	59.9
21 Jun	23	13.9
Event total	75.8	90.9
All-time daily record	95.3 (15 Jul 1927)	59.9 (20 Jun 2013)

We primarily utilize an ingredients-based methodology for flash flooding proposed by Doswell et al. (1996), in which the ingredients are lift (trigger), moisture, and instability. We will show that a complex multiscale evolution in the 10 days prior and the persistence of flash flood ingredients on multiple scales led to the 19–21 June extreme rainfall event. The remainder of the paper is organized as follows: Section 2 presents data used, section 3 provides an event overview, section 4 examines the antecedent large-scale flow evolution 7–10 days prior to the event, and section 5 provides an ingredients-based synoptic–dynamic analysis of the extreme rainfall event. A concluding discussion and overview of planned future work are given in section 6.

2. Data

Precipitation data presented in Table 1 were obtained from the Environment Canada (EC) historical climate database (Environment Canada 2014d). Streamflow data (Fig. 2) were saved in real time using the Alberta Environment and Sustainable Resource Development website (Alberta Environment 2013).

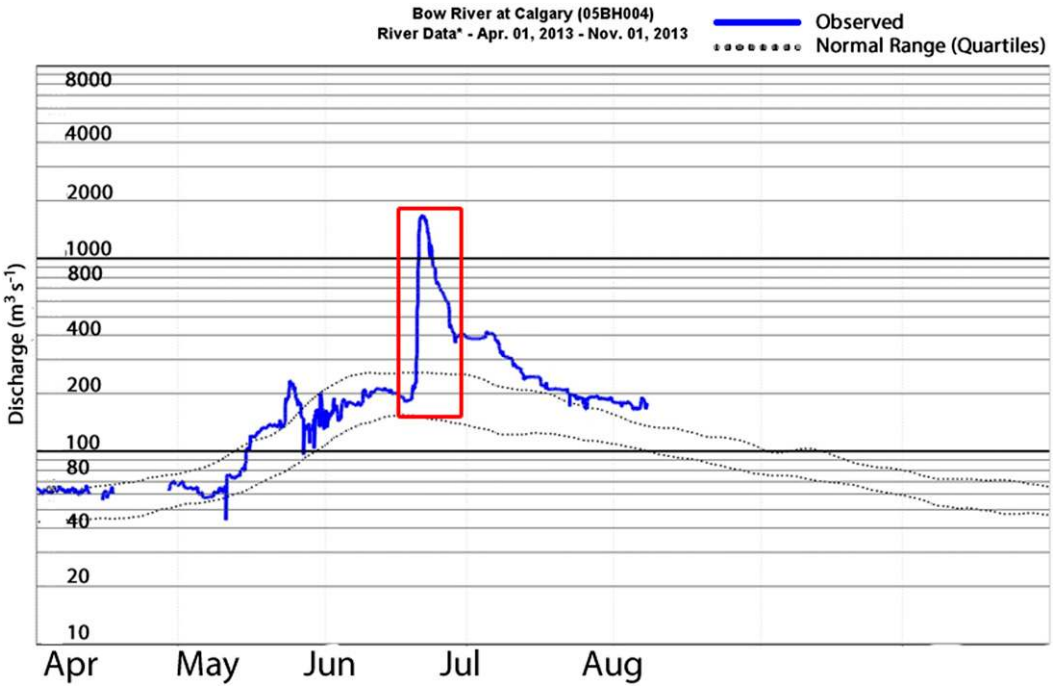

FIG. 2. Streamflow ($m^3 s^{-1}$) on the Bow River at downtown Calgary, retrieved from Alberta Environment (Alberta Environment 2013). The approximate time period of the Alberta flood is indicated by the red box, and the normal range (25th and 75th percentiles) is shown by the dashed black lines.

Radar data were obtained using the EC historical radar database (Environment Canada 2014c). The data are from the Strathmore, Alberta (CXSM), radar, approximately 50 km east-northeast of Calgary International Airport. EC radars are C-band radars with a wavelength of 5 cm and a beamwidth of 0.65° (Environment Canada 2014a).

The gridded precipitation data shown in Fig. 3 were produced using the EC Canadian Precipitation Analysis (CaPA), which has a 15-km grid spacing and 6-h temporal resolution (Mahfouf et al. 2007), and was accessed through the Data Access Integration website (Climat-Quebec 2014). The CaPA has been shown to be the best available gridded precipitation dataset for Canada (Mahfouf et al. 2007; Milrad et al. 2009a).

For the synoptic–dynamic analysis, we primarily utilized the National Centers for Environmental Prediction Climate Forecast System Reanalysis (CFSR), which is run on T382 spectral resolution (~38 km) and was obtained on a 0.5° global grid, with a 6-h temporal resolution (Saha et al. 2010). We also used the North American Regional Reanalysis (NARR), which has a grid spacing of 32 km, and 3-h temporal resolution (Mesinger et al. 2006).

Hovmöller diagrams were produced using the NOAA/Earth System Research Laboratory time-section plots (http://www.esrl.noaa.gov/psd/map/time_plot/); we used Global Reanalysis 1 (Kalnay et al. 1996) as the plotting dataset. Finally, backward air parcel trajectories were calculated using the NOAA/Air Resources Laboratory Hybrid Single-Particle Lagrangian Integrated Trajectory model (HYSPLIT; Draxler and Rolph 2012), and we chose the National Centers for Environmental Prediction global data assimilation scheme (Kanamitsu 1989) as the trajectory dataset, based on its availability and global grid (1° grid spacing).

All calculations and analyses in this study, except for the air parcel trajectories and Hovmöller diagrams, are displayed using the General Meteorological Package (GEMPAK), version 7.0.0, updated from the original package devised by Koch et al. (1983).

3. Event overview

The rainfall in southern Alberta began around 0000 UTC 20 June 2013. Local climatological data in Alberta (including precipitation) are based on midnight–midnight local time, so the dates presented in Table 1 are in mountain daylight time (MDT). For reference, midnight–midnight MDT is 0600–0600 UTC. In Table 1, precipitation totals are given for both the Calgary International Airport (CYYC) and Banff (CWZG), which is located 140 km west-northwest of CYYC. CWZG was chosen as the station with available data most representative of precipitation in the foothills, although unofficial rainfall

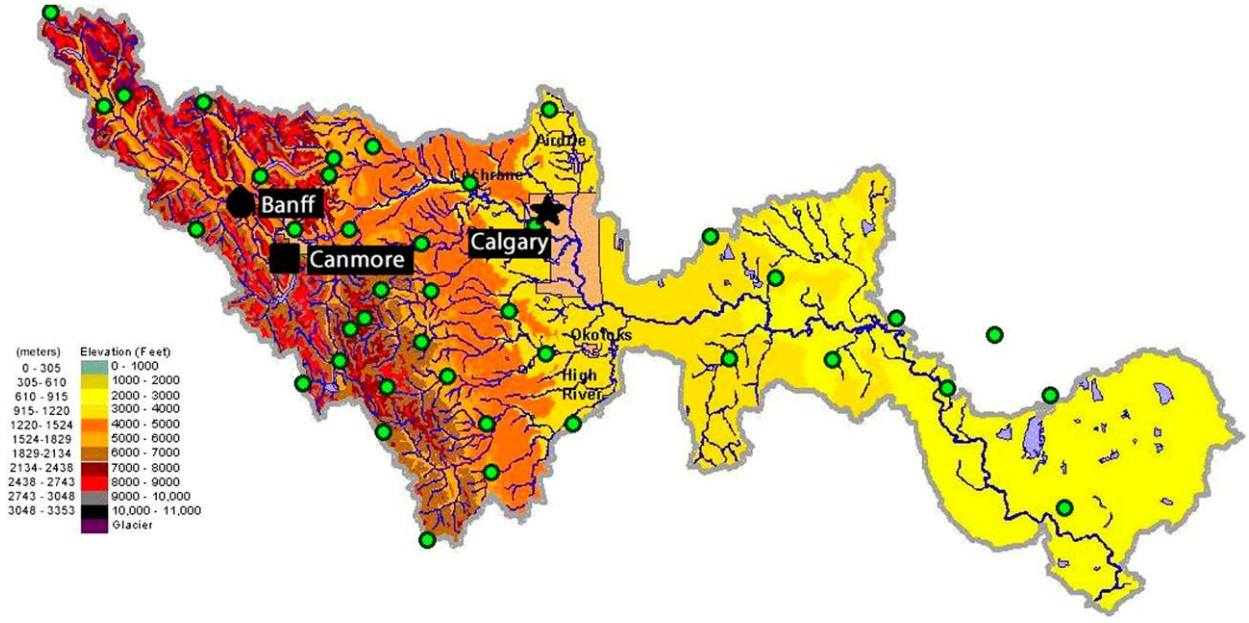

FIG. 3. Taken from the Alberta Environment River basin website (Alberta Environment 2013), elevation map of the Bow River basin in southern Alberta. For reference, the approximate locations of the Calgary International Airport, Banff, and Canmore are labeled and marked on each panel with a black star, circle, and square, respectively. The green circles indicate streamflow gauges throughout the basin.

estimates and damage were higher (Environment Canada 2014b) slightly farther south near Canmore (120 km west of CYYC).

From 0000 to 0600 UTC 19 June, CYYC received only 7.8 mm of precipitation, while CWZG recorded more than twice that with 17.1 mm (Table 1). The heaviest precipitation fell from 0600 UTC 20 June to 0600 UTC 21 June, as CYYC reported 45 mm, while 59.9 mm accumulated at CWZG. The all-time record for daily precipitation at CYYC is 95.3 mm (15 July 1927), while CWZG broke their all-time daily record (55 mm on 18 June 2005). The June daily precipitation record at CYYC is 79.2 mm (1 June 1932). For event totals, CYYC and CWZG reported 75.9 and 90.8 mm, respectively (Table 1). The 17–18 June 2005 event at CWZG did have a slightly higher 2-day total of 106.5 mm.

Figure 2 shows the rapid increase in streamflow in the Bow River at Calgary on 20 June. In less than 12 h, discharge increased from 200 $m^3 s^{-1}$ to a record level (Environment Canada 2014b) of approximately 1700 $m^3 s^{-1}$ and did not begin to subside for a couple of days. Similar increases were also seen on the nearby Elbow River (now shown). Doswell et al. (1996) and Maddox et al. (1978, 1979, 1980) noted that orography is typically a large contributor to Front Range flash floods, both meteorologically (trigger) and hydrologically (streamflow). This was particularly true in the 1976 Big Thompson flood in Colorado (Maddox et al. 1978; Caracena et al. 1979) and more recently the 2013 Great Colorado flood (e.g., Gochis et al. 2015). As heavy rainfall fell in the Canmore and Banff areas at elevations of 2133–2743 m (7000–9000 ft), streamflow in the Elbow and Bow Rivers increased rapidly (e.g., Fig. 2) and flowed 1219–1524 m (4000–5000 ft) downhill toward Calgary (Figs. 1, 2). Many areas suffered damage, not so much due to in situ rainfall as to a rapid rise in downhill-moving streamflow.

Figure 4 shows that both the Calgary area and the foothills received large amounts of precipitation during each 6-h period on 20 June, including 30–40 mm in the foothills between 1200 and 1800 UTC 20 June (Fig. 4c). As in the Big Thompson (Colorado) and Rapid City (South Dakota) floods (Maddox et al. 1978), and the 2013 Great Colorado flood (Gochis et al. 2015), the Alberta flood was characterized by relatively steady moderate to heavy rainfall over a long time period, maximized from 0600 to 1800 UTC 20 June. The temporal and intensity characteristics of the rainfall event mesh with the conclusions of Doswell et al. (1996); that is, in order to get a high-impact flash flood event, large rainfall rates need to occur over a long duration.

Figure 5 shows heavy rainfall echoes were evident near Canmore and Banff starting at 0000 UTC 20 June (Fig. 5a), and they became more widespread by 0300 UTC, repeatedly moving (training) over the foothills (i.e., Canmore and Banff; Fig. 5b). Moderate to heavy rainfall finally moved into Calgary by 0600 (Fig. 5c) and 0900 UTC (Fig. 5d). In the foothills, moderate to heavy precipitation persisted over the area through 1200 UTC 21 June

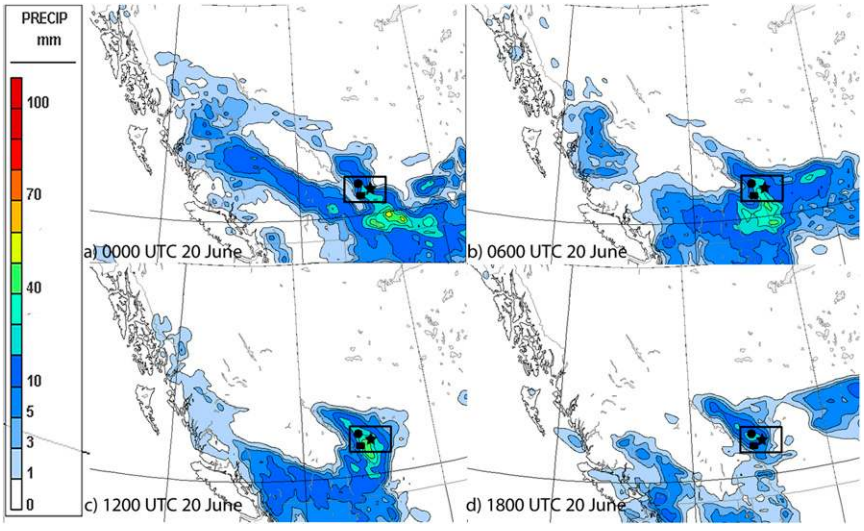

FIG. 4. CaPA 6-h precipitation totals (mm) starting at the time indicated on each panel: (a) 0000–0600 UTC 20 Jun, (b) 0600–1200 UTC 20 Jun, (c) 1200–1800 UTC 20 Jun, and (d) 1800 UTC 20 Jun–0000 UTC 21 Jun. For reference, the approximate locations of the Calgary International Airport, Banff, and Canmore are marked on each panel with a black star, circle, and square, respectively. The black box represents the approximate area of the Bow River basin, detailed in Fig. 3.

(Fig. 5i), resulting in considerably higher precipitation totals than in Calgary (Table 1).

Maddox et al. (1978, 1979) and Schumacher and Johnson (2006) found that flash floods east of the Rocky Mountains are fairly common in the warm season (particularly June–August) and that the heaviest precipitation generally occurs in the evening and overnight hours. In the Front Range flash floods, upslope (westward)-moving convective echoes within a quasi-stationary MCS often backbuild on the east or southeastern (upstream) side (Maddox et al. 1978); Schumacher and Johnson (2005) more generally classified these MCSs as Type BB (backbuilding). These characteristics are shown in the radar evolution of the precipitation corresponding to the Alberta flood (Fig. 5), and also were observed during the 2013 Colorado flood (Gochis et al. 2015). Rainfall began in the early evening MDT (0000 UTC 20 June) and some of the heaviest amounts were recorded overnight (Figs. 4, 5). Even when the precipitation coverage was spatially limited (e.g., 1800 UTC 20 June), rainfall was still observed over Canmore and Banff (Fig. 5f), with new echoes upstream (south-southeast), moving north-northwest.

4. Antecedent large-scale conditions

At 0000 UTC 11 June, 9 days before event onset, an upper-tropospheric ridge [marked by warm potential temperature on the dynamic tropopause (DT); Fig. 6a] is present over the western North Pacific just south of Japan. At the same time, Tropical Storm Yagi (Fig. 6a) is moving northward through the ridge environment toward Japan. Recent work (e.g., Archambault et al. 2013) has noted that recurving and extratropically transitioning western North Pacific tropical cyclones can sometimes have an impact on the downstream upper-tropospheric flow pattern through jet streak intensification and downstream development of a Rossby wave train. Although the Alberta flood was preceded by an antecedent Rossby wave train over the North Pacific (Figs. 6, 7), there is no evidence suggesting that Tropical Storm Yagi played a large role in its development. Yagi remained underneath the large-scale DT ridge environment as it meandered to the southeast of Japan.

Over East Asia, strong baroclinic cyclogenesis precedes intensification of the downstream ridge located north of Japan at 0000 UTC 13 June (Fig. 6b), likely due to a combination of diabatic heating and warm-air advection (WAA; e.g., Milrad et al. 2009a). Subsequently, downstream flow amplification is evident across the North Pacific. Between 0000 UTC 13 June and 0000 UTC 15 June, a cyclonic DT disturbance is located downstream of the initial ridge (anticyclonic DT disturbance) at 0000 UTC 13 June (Fig. 6b). A new anticyclonic DT disturbance appears farther downstream over the Aleutian Islands at 0000 UTC 15 June (Fig. 6c). By 0000 UTC 17 June, the anticyclonic DT disturbance becomes removed from the midlatitude westerly flow and a pronounced cutoff ridge is observed over Alaska (Fig. 6d),

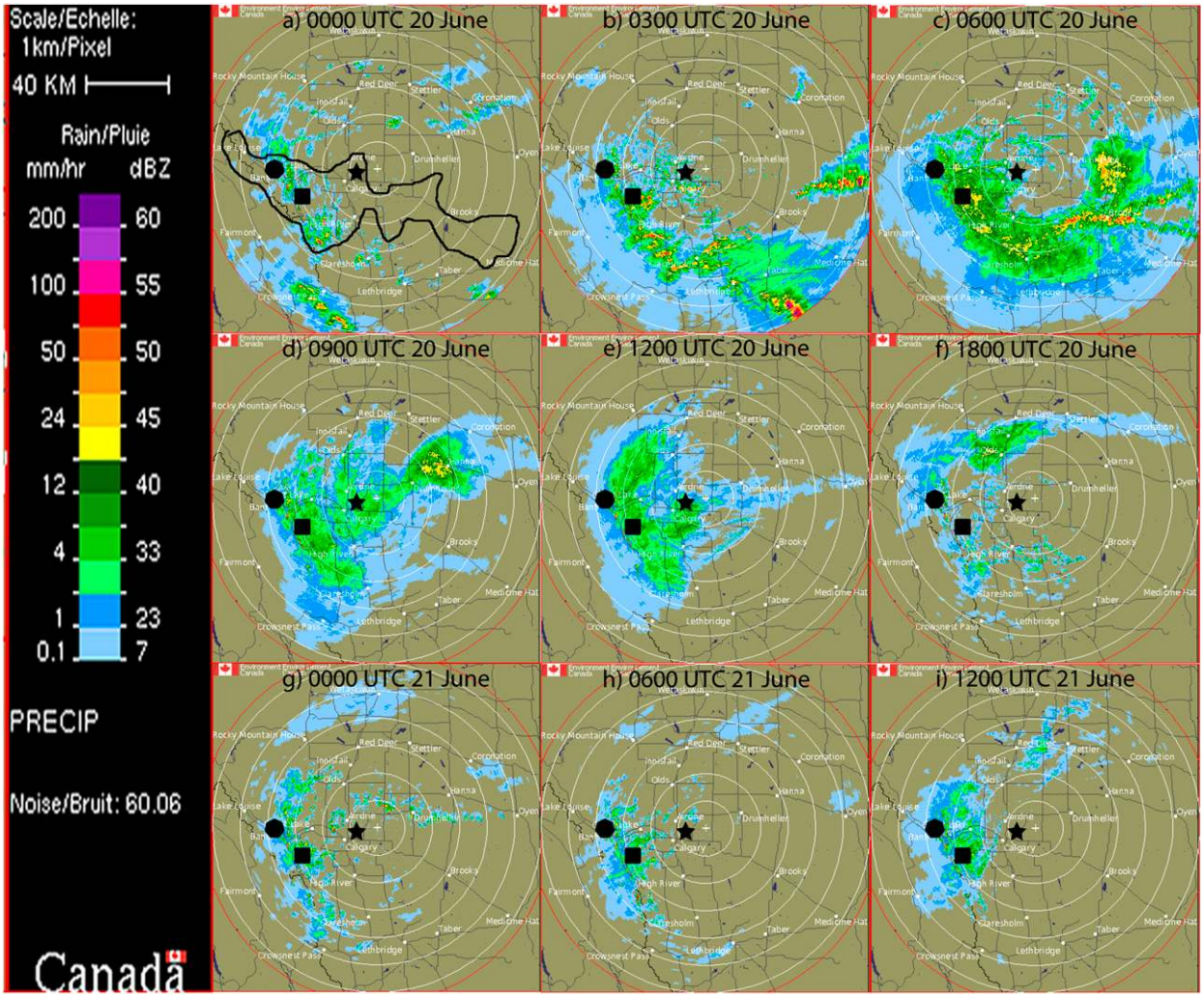

FIG. 5. EC radar imagery from the Strathmore (Calgary) radar at (a) 0000 UTC 20 Jun, (b) 0300 UTC 20 Jun, (c) 0600 UTC 20 Jun, (d) 0900 UTC 20 Jun, (e) 1200 UTC 20 Jun, (f) 1800 UTC 20 Jun, (g) 0000 UTC 21 Jun, (h) 0600 UTC 21 Jun, and (i) 1200 UTC 21 Jun. For reference, the approximate locations of the Calgary International Airport, Banff, and Canmore are marked on each panel with a black star, circle, and square, respectively. An outline of the Bow River basin (Fig. 3) is drawn in solid black in (a).

setting up a Rex block (blocking ridge to the north, cutoff cyclone to the south; Rex 1950) in the northeastern North Pacific.

To further investigate downstream flow amplification, Fig. 7 shows Hovmöller diagrams of meridional wind and IWV anomalies (with respect to a 1981–2010 climatology) at 50°N (Figs. 7a,c) and 60°N (Figs. 7b,d). Figure 7a shows a Rossby wave train starting over East Asia on 11–12 June, with downstream flow amplification evident to the west coast of North America by 18 June. Farther north, the Alaskan ridge is very evident on 15 June (Fig. 7b), and the wave pattern is more stagnant than at 50°N (Fig. 7a), supporting our observation of a Rex block. This evolution highlights the importance of baroclinic development in downstream flow amplification.

In accordance with the strong southerly flow in the North Pacific just east of the international date line (Figs. 7a,b), a +16-mm IWV anomaly is observed from 14 to 17 June as far north as the Gulf of Alaska (Figs. 7c,d). We will show later that this was associated with a pronounced AR of subtropical moisture transport to polar latitudes. Figure 7c also shows a +10-mm IWV anomaly on 19–20 June near southern Alberta (115°W), ahead of weakly anomalous southerly flow; these features are located ahead of a 500-hPa cutoff cyclone and on the western periphery of a subtropical anticyclone, which we explore in the next section.

At 0000 UTC 11 June (Fig. 8a), a relatively narrow subtropical anticyclone is located in the central North Pacific, while IWV values over the Aleutian Islands and

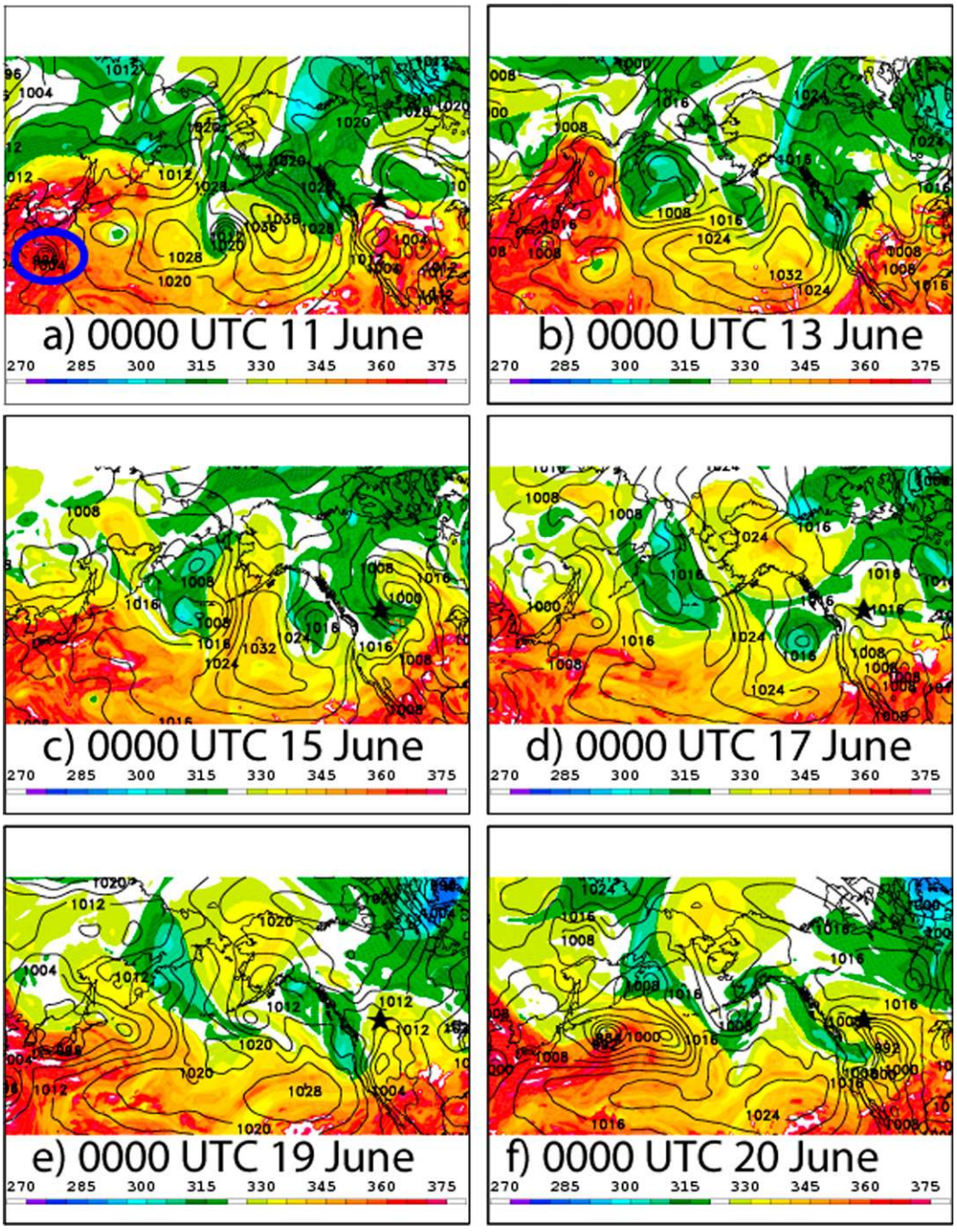

FIG. 6. CFSR potential temperature (K, shaded) on the DT (2-PVU surface) and MSLP (hPa, contours) for (a) 0000 UTC 11 Jun (b) 0000 UTC 13 Jun, (c) 0000 UTC 15 Jun, (d) 0000 UTC 17 Jun, (e) 0000 19 Jun, and (f) 0000 UTC 20 Jun. The approximate location of the Calgary International Airport is marked with a black star in each panel and Tropical Storm Yagi is circled in blue in (a).

Alaska are generally small (<20 mm). However, by 0000 UTC 13 June, the aforementioned anticyclone has elongated toward the west (Fig. 8b), and by 0000 UTC 15 June, a strong lower-tropospheric pressure gradient (Figs. 6c, 8c) is present between the 1004-hPa cyclone in the western Aleutians and the 1032-hPa subtropical anticyclone centered near Hawaii. This helps to initiate strong poleward moisture transport (Figs. 8c,d) from the subtropics into Alaska. The IWV values in the moisture plume exceed 40 mm—more than double the 20-mm threshold

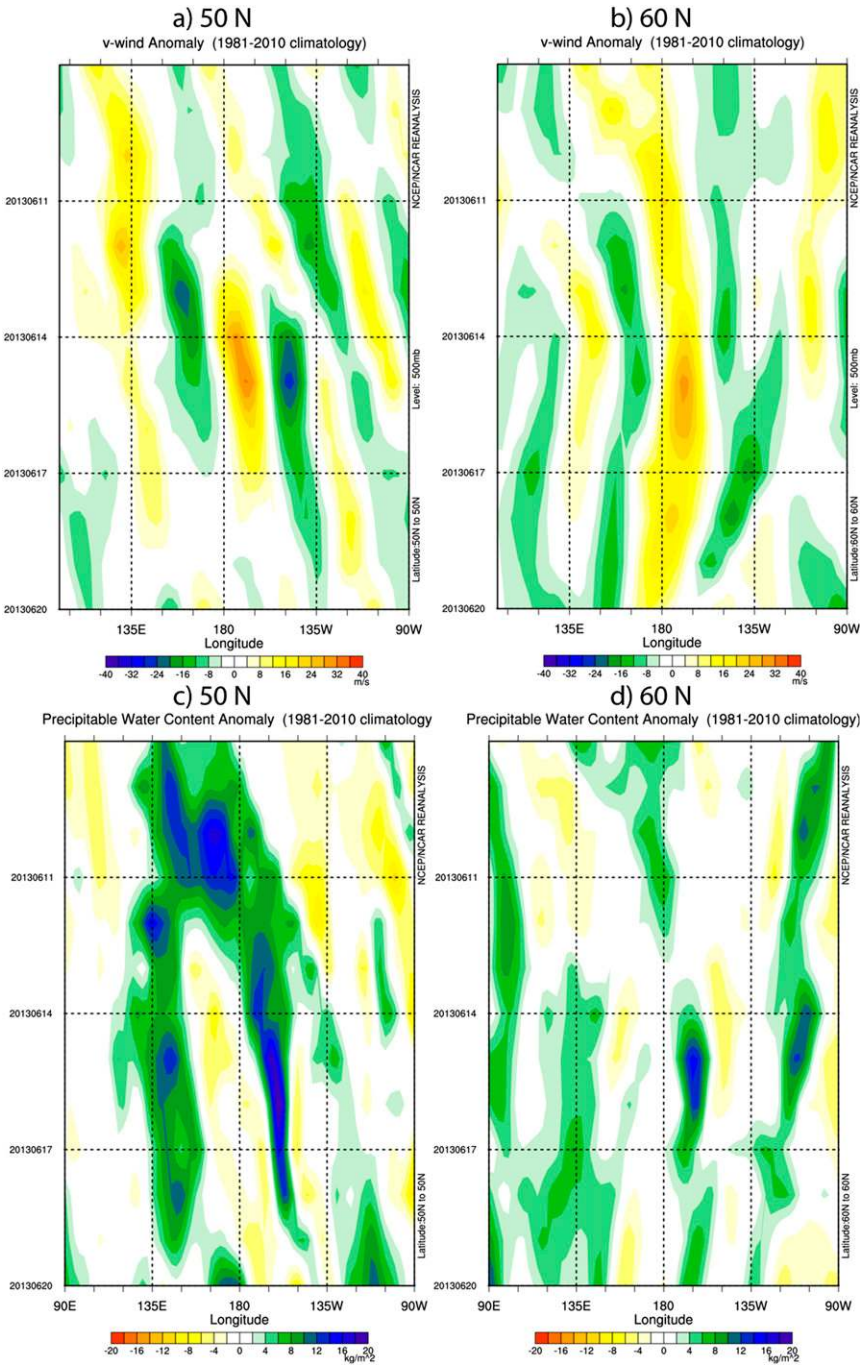

FIG. 7. From 0000 UTC 8 Jun to 0000 UTC 20 Jun 2013, Hovmöller diagrams of (a),(b) 500-hPa meridional wind anomalies and (c),(d) IWV (precipitable water, mm) anomalies, from 100°E to 90°W, centered at (a),(c) 50° and (b),(d) 60°N. Images provided by the NOAA/Earth System Research Laboratory's Physical Sciences Division (http://www.esrl.noaa.gov/psd/).

for an AR defined by Ralph et al. (2004, 2011). Strong ARs (i.e., "Pineapple Express") into Alaska and northwestern Canada are often associated with large amounts of precipitation along the coastal mountain ranges (e.g., Lackmann and Gyakum 1996; Roberge et al. 2009), concomitant with moisture flux convergence (MFC; e.g., Junker et al. 1999; Ralph et al. 2011; Rutz et al. 2014). CFSR precipitation grids (not shown) suggest that most precipitation associated with this AR fell in the Aleutians and southwest coast of Alaska, as MFC occurred over the

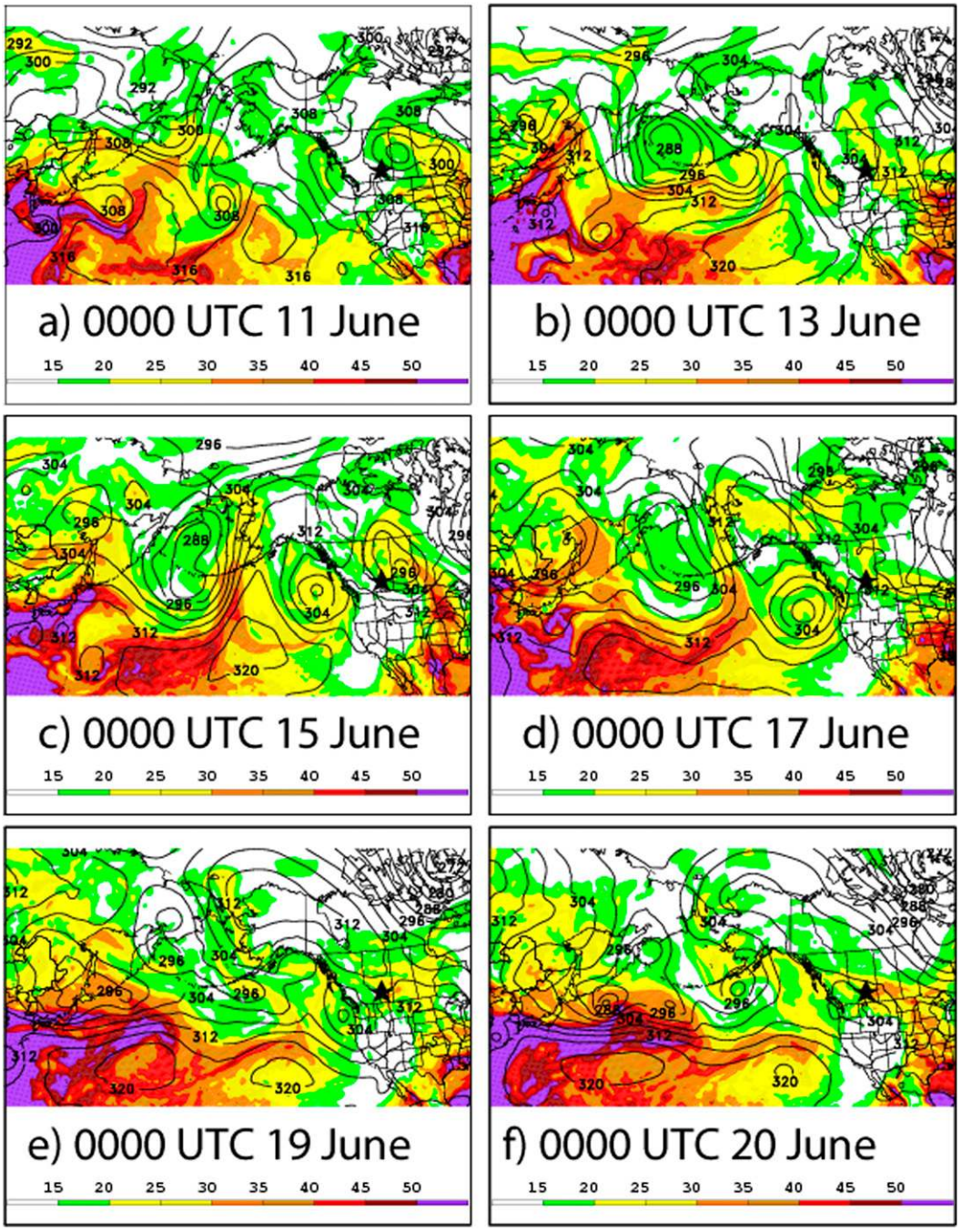

FIG. 8. As in Fig. 6, but for IWV (mm, shaded) and 700-hPa geopotential height (dam, solid contours). The approximate location of the Calgary International Airport is marked with a black star in each panel.

elevated terrain. Analyses of potential vorticity advection by the irrotational wind (e.g., Archambault et al. 2013; not shown) find that negative potential vorticity advection is located near and just downstream of the heaviest precipitation, as the Alaskan ridge intensified from 0000 UTC 15 June to 0000 UTC 17 June (Figs. 6c,d). Therefore, we suggest that the latest heat release from heavy precipitation associated with this AR likely helped to amplify the anticyclonic DT disturbance over Alaska by 0000 UTC 17 June (Fig. 6d). This cutoff ridge (Figs. 6d–f) was then associated with record-breaking maximum temperatures over Alaska in mid-June.

The Rex block at 0000 UTC 17 June (Fig. 6d) consists of the Alaskan ridge north of a cyclonic DT disturbance

located west of British Columbia. In order for the west coast cyclonic DT disturbance (Figs. 6c–f) to progress eastward, the Rex block in the northeastern North Pacific must break down. The key driver of destroying the block appears at 0000 UTC 17 June (Fig. 6d), when a strong cyclonic DT disturbance moves across the northern periphery of the Alaskan ridge. By 0000 UTC 19 June, the cyclonic DT disturbance interrupts the easterly flow in the middle of the Rex block (Fig. 6e), allowing the original cyclonic DT disturbance along the southern British Columbia coast to begin to move eastward onto the continent.

It is evident that the subtropical anticyclone (Figs. 6c, 8c) and the Alaskan ridge (Figs. 6d, 8d) played important roles in moisture transport. This finding is interesting in the context of Pfahl and Wernli (2012), who found that cyclones account for the large majority of extreme precipitation events. We suggest that while this may be explicitly true, the evolution of the planetary- and synoptic-scale patterns prior to an extreme precipitation event is often more complicated and nuanced, with anticyclones frequently playing an important role in moisture transport and airmass modification (e.g., Newman et al. 2012; Milrad et al. 2014a).

5. Synoptic–dynamic characteristics

Gyakum (2008) proposed that for a given amount of ascent, the precipitation rate is dependent on the temperature and moisture (stability) characteristics of the air mass. Milrad et al. (2014a) used this idea to help partition heavy precipitation events from moderate and light events. We will refer to both the Doswell et al. (1996) and Gyakum (2008) approaches throughout the remainder of the paper.

a. Lift

The cyclonic DT disturbance finally moves into British Columbia and Washington by 0000 UTC 19 June (Fig. 9a). In response, a lee mean sea level pressure (MSLP) cyclone develops over southern Montana (Figs. 9a,b). Between 1200 UTC 19 June and 0000 UTC 20 June (Figs. 9b–d), the MSLP cyclone deepens 12 hPa, which helps to create strong low-level easterly (upslope) geostrophic flow throughout southern Alberta and Saskatchewan (Fig. 9d). Strong low-level geostrophic easterlies continue through 0600 and 1200 UTC 20 June (Figs. 9e–f), during the time of heaviest precipitation. Prolonged easterly upslope flow in Front Range flash flood events was also observed by Maddox et al. (1978, 1979, 1980) and Gochis et al. (2015). Finally, note that the upper-tropospheric (DT) pattern from 1800 UTC 19 June (Fig. 9c) onward (Figs. 9d–f) strongly resembles that of the 2013 Great Colorado flood (Gochis et al. 2015), with a large ridge located north of a cutoff cyclone (Rex block). The stagnant synoptic-scale pattern contributed to the persistence and duration of the rainfall. To that end, Maddox et al. (1980) classified upper-tropospheric Rex blocks as "type 1" in their flash flooding synoptic composites.

One advantage to using DT diagnostics is that potential temperature on the DT is conserved for adiabatic processes. As such, we can ascribe a Lagrangian increase in potential temperature on the DT to diabatic heating as a result of latent heat release from heavy precipitation (e.g., Milrad et al. 2009a). A signature of diabatic heating is evident over Alberta after event onset (0000–1200 UTC 20 June; Figs. 9d–f), as the potential temperature increases approximately 30 K. At 1200 UTC 20 June, backward trajectories and analyses of potential temperature advection on the DT (not shown) confirm that the observed increase in potential temperature in southern Alberta was overwhelmingly not due to positive theta advection from a source region and that it was therefore mostly associated with in situ diabatic heating. By 0600 and 1200 UTC 20 June (Figs. 9e,f), the ridge acquires a pronounced negative tilt, thins, and wraps cyclonically, strongly resembling the "bent-back ridge" pattern observed in the flash flood composites of Maddox et al. (1978).

To help diagnose forcing for ascent in this section, we use the **Q**-vector form of the inviscid, adiabatic quasi-geostrophic (QG) omega equation:

$$\left(\nabla_p^2 + \frac{f_o^2}{\sigma}\frac{\partial^2}{\partial p^2}\right)\omega = -2\nabla_p \cdot \mathbf{Q}, \tag{1}$$

where f_o is the constant Coriolis parameter (s^{-1}), σ is the static stability parameter ($m^2 s^{-2} Pa^{-2}$), ω is the vertical velocity ($Pa\,s^{-1}$), and the sense of the vertical motion is related to the divergence of the **Q** vector. This was expressed by Hoskins et al. (1978, p. 34): "in quasi-geostrophic theory...vertical velocity is forced solely by the divergence of Q." Thus, areas of **Q**-vector convergence are associated with QG forcing for ascent.

The **Q** vector can be separated into its along-isentrope ($\mathbf{Q}_s$) and across-isentrope ($\mathbf{Q}_n$) components, originally devised by Keyser et al. (1988, 1992) and later discussed by Martin (1999, 2006a,b):

$$\mathbf{Q}_s = \left[\frac{\mathbf{Q}\cdot(\hat{k}\times\nabla\theta)}{|\nabla\theta|}\right]\frac{\hat{k}\times\nabla\theta}{|\nabla\theta|} \quad \text{and} \tag{2}$$

$$\mathbf{Q}_n = \left(\frac{\mathbf{Q}\cdot\nabla\theta}{|\nabla\theta|}\right)\frac{\nabla\theta}{|\nabla\theta|}. \tag{3}$$

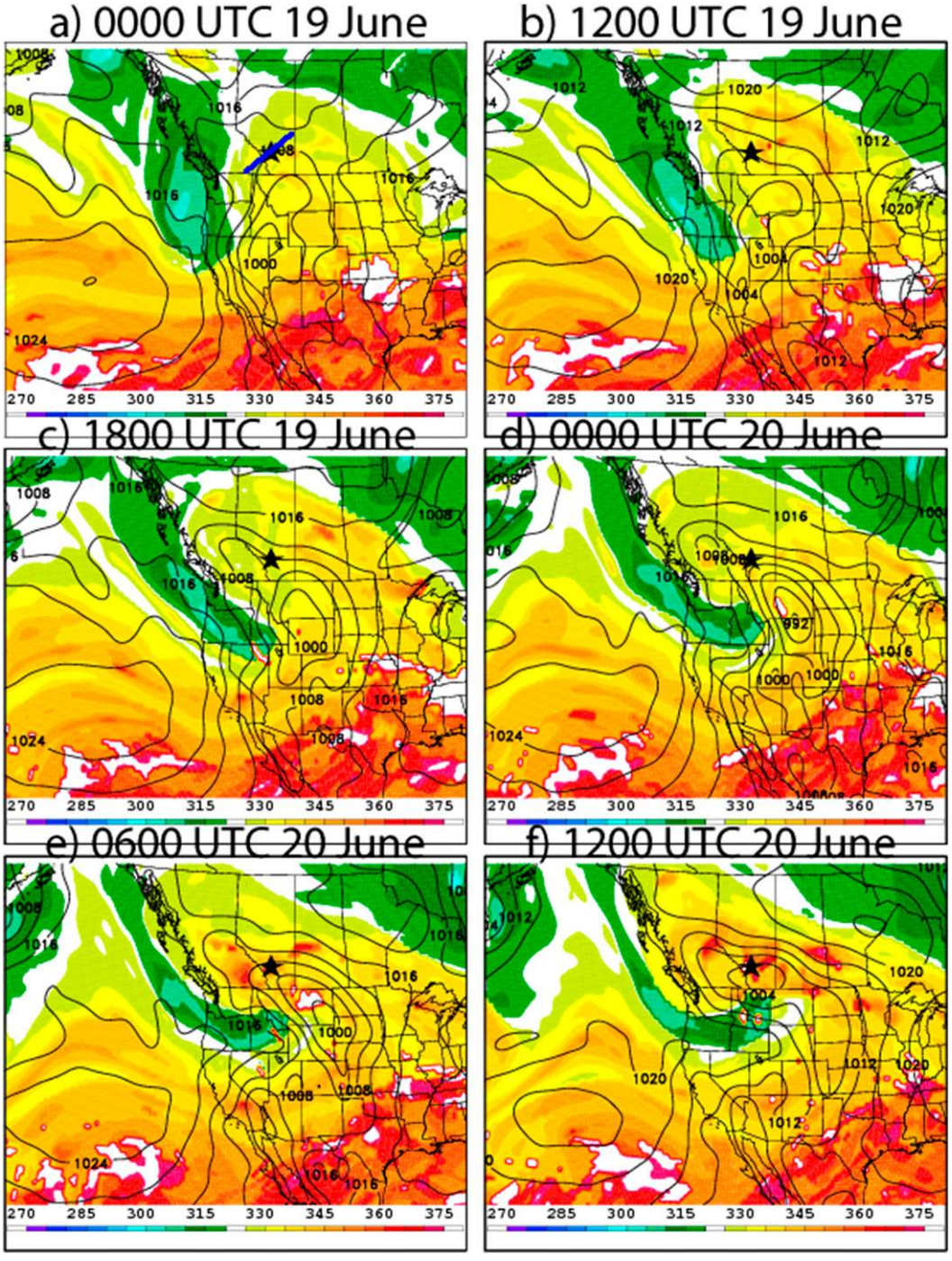

FIG. 9. CFSR potential temperature (K, shaded) on the DT (2-PVU surface) and MSLP (hPa, contours) for (a) 0000 UTC 19 Jun, (b) 1200 UTC 19 Jun, (c) 1800 UTC 19 Jun, (d) 0000 UTC 20 Jun, (e) 0600 UTC 20 Jun, and (f) 1200 UTC 20 Jun. The blue line in (a) represents the cross-sectional area in Figs. 11 and 16. The approximate location of the Calgary International Airport is marked with a black star in each panel.

Keyser et al. (1988, 1992), Martin (1999, 2006a,b), and Milrad et al. (2010a, 2014a) used the components of $\mathbf{Q}$ to diagnose different forcing processes for ascent; $\mathbf{Q}_s$ convergence ($\nabla_p \cdot \mathbf{Q}_s < \mathbf{0}$) is representative of forcing for ascent associated with the rotation of the potential temperature gradient vector, and $\mathbf{Q}_n$ convergence ($\nabla_p \cdot \mathbf{Q}_n < \mathbf{0}$) corresponds to forcing for ascent associated with the change in the magnitude of the potential temperature

gradient (Keyser et al. 1992). As Milrad et al. (2014a) stated, $\mathbf{Q}_s$ convergence is representative of cyclonic vorticity advection (CVA) by the thermal wind, while $\mathbf{Q}_n$ convergence is associated with geostrophic frontogenesis. We note that in accordance with the **Q**-vector form of the QG omega equation [Eq. (1)], no aspect of **Q** accounts for orographic forcing for ascent.

At 0000 UTC 20 June, Figs. 10a and 10b show that $\mathbf{Q}_s$ divergence is observed from Calgary southward, while strong $\mathbf{Q}_n$ convergence is observed over the foothills flood region, suggesting mostly frontogenesis. Overall, there is QG forcing for ascent in the flood region (Fig. 10c). The reverse is true at both 0600 (Figs. 10d,e) and 1200 UTC 20 June (Figs. 10g,h), when both $\mathbf{Q}_s$ convergence and $\mathbf{Q}_n$ divergence are observed. However, there is still net **Q** convergence at both times (Figs. 10f,i), indicating QG ascent over the flood region, albeit weaker than at 0000 UTC 20 June (Fig. 10c). Plots of total frontogenesis (not shown) show that frontogenesis did not play a major role in producing ascent at the times of heaviest precipitation (i.e., 0600 and 1200 UTC 20 June).

Both Maddox et al. (1978) and Junker et al. (1999) found that of QG mechanisms for ascent in flash floods, lower-tropospheric WAA is typically of a larger magnitude than differential CVA. To that end, strong WAA (isobars nearly perpendicular to thickness contours) is present on the north side of the lee MSLP cyclone (Figs. 10b,e,h). Calculations of WAA and CVA (not shown) indicate that at 0600 and 1200 UTC 20 June, differential CVA in the heavy rainfall region is small to nonexistent, while WAA is relatively large. This suggests that the $\mathbf{Q}_s$ convergence in Figs. 10d and 10g is primarily associated with WAA. Finally, the geostrophic easterlies (Figs. 10b,e,h) suggest that orography also likely contributed to the total forced ascent, especially at later times (e.g., 1200 UTC 20 June). Flesch and Reuter (2012), Brimelow and Reuter (2005), and Maddox et al. (1978) also found this for flood events in Alberta and regions of similar terrain.

To assess the contribution of orography in producing ascent, Fig. 11 shows a southwest–northeast cross section (blue line in Fig. 9a) comparing NARR upward vertical motion (ω, solid contours) to ascent produced by the orography (ω_{oro}), defined by

$$\omega_{\text{oro}} = -\rho g(\mathbf{v} \cdot \nabla z), \tag{4}$$

where ρ is density, g is the gravitational constant, and $\mathbf{v} \cdot \nabla z$ is representative of vertical velocity in height coordinates (i.e., w) caused by the terrain. We used NARR data to produce the cross sections because it better represents the local terrain, although the stability metrics in the CFSR were very similar (not shown). Figure 11 shows that prior to precipitation onset (0000 UTC 20 June), orographic ascent was present at 1200 and 1800 UTC 19 June (Figs. 11b,c) within low-level easterly flow, which may have helped to saturate the atmosphere over the flood region. During the main precipitation period (0000–1800 UTC 20 June; Figs. 11d–f), orographic ascent is a contributor to the total ascent at 0000 UTC 20 June (Fig. 11d) and even more so at 1200 UTC 20 June (Fig. 11f). This is particularly evident over the foothills west-southwest of Calgary, within very strong low-level easterly flow (Fig. 11f). We can therefore conclude that orographic ascent, working in concert with the QG ascent-forcing processes (primarily WAA, not CVA), likely helped to enhance and prolong precipitation, especially later in the event (e.g., 1200 UTC 20 June).

b. *Moisture*

Throughout this section, we use numerous variables to diagnose moisture sources, transport, and convergence. First, IWV (columnar precipitable water) is defined by

$$\text{IWV} = \frac{1}{g\rho} \int_{\text{surface}}^{300\,\text{hPa}} q \, dp, \tag{5}$$

where g is the gravitational constant, ρ is the density of liquid water, q is the specific humidity, and p is the pressure. The integrated vapor transport (IVT; e.g., Moore et al. 2012) is defined by

$$\text{IVT} = \frac{1}{g} \int_{1000\,\text{hPa}}^{300\,\text{hPa}} q\mathbf{v}_h \, dp, \tag{6}$$

where $\mathbf{v}_h$ is the horizontal wind vector. Finally, vertically integrated 1000–300-hPa MFC (e.g., Banacos and Schultz 2005) is defined in vector form by

$$\text{MFC} = -\nabla \cdot (\text{IVT}). \tag{7}$$

Figure 12 shows 850-hPa θ_e, select values of positive θ_e advection, and wind. We caution that because 850 hPa is located close to the surface in parts of the flood region, a small diurnal cycle in θ_e is evident from 0000 to 1200 UTC 19 June (Figs. 12a,b). However, the diurnal cycle does not impact our conclusions regarding θ_e advection. Positive θ_e advection is evident over southern Alberta as early as 0000 UTC 19 June (Fig. 12a), and it increases markedly within the easterly upslope flow by 0000 UTC 20 June (Fig. 12d), broadly continuing through 0600 and 1200 UTC (Figs. 12e,f). Junker et al. (1999) positively correlated regions of positive θ_e advection to WAA, which is observed throughout the flood region from 0000 to 1200 UTC 20 June (Figs. 10b,e,h).

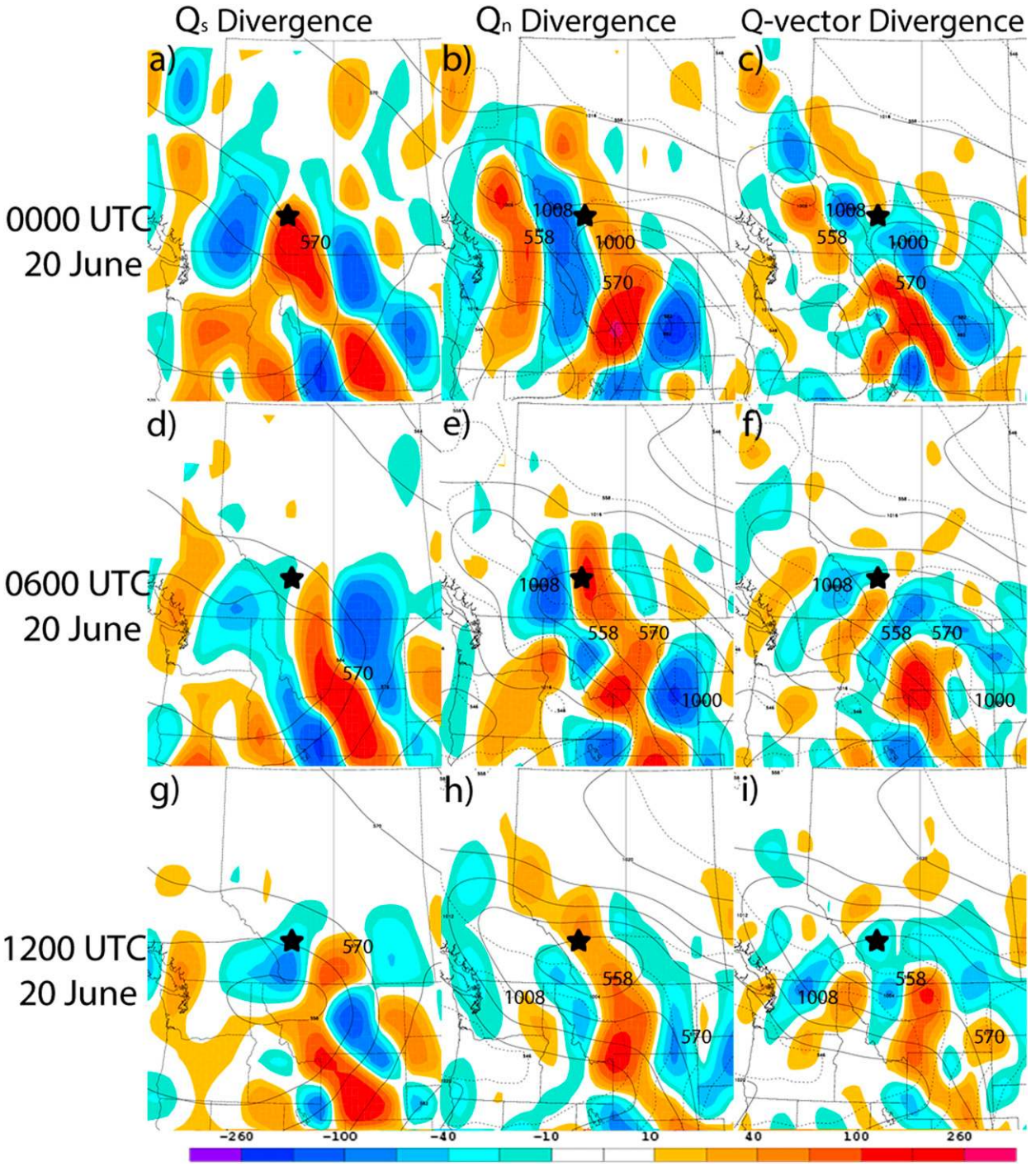

FIG. 10. For (a)–(c) 0000, (d)–(f) 0600, and (g)–(i) 1200 UTC 20 Jun: (left) 1000–500-hPa layer-averaged $\mathbf{Q}_s$ divergence ($\times 10^{-16}$ K m^{-2} s^{-1}, shaded cool colors for convergence) and 500-hPa geopotential height (solid contours every 6 dam, 570-dam contour labeled in bold); (middle) 1000–500-hPa layer-averaged $\mathbf{Q}_n$ divergence ($\times 10^{-16}$ K m^{-2} s^{-1}, shaded cool colors for convergence), MSLP (solid contours every 4 hPa, select values labeled in bold), and 1000–500-hPa thickness (dashed contours every 6 dam, select values labeled in bold); and (right) 1000–500-hPa layer-averaged total $\mathbf{Q}$-vector divergence ($\times 10^{-16}$ K m^{-2} s^{-1}, shaded cool colors for convergence), MSLP (solid contours every 4 hPa, select values labeled in bold), and 1000–500-hPa thickness (dashed contours every 6 dam, select values labeled in bold). The approximate location of the Calgary International Airport is marked with a black star in each panel.

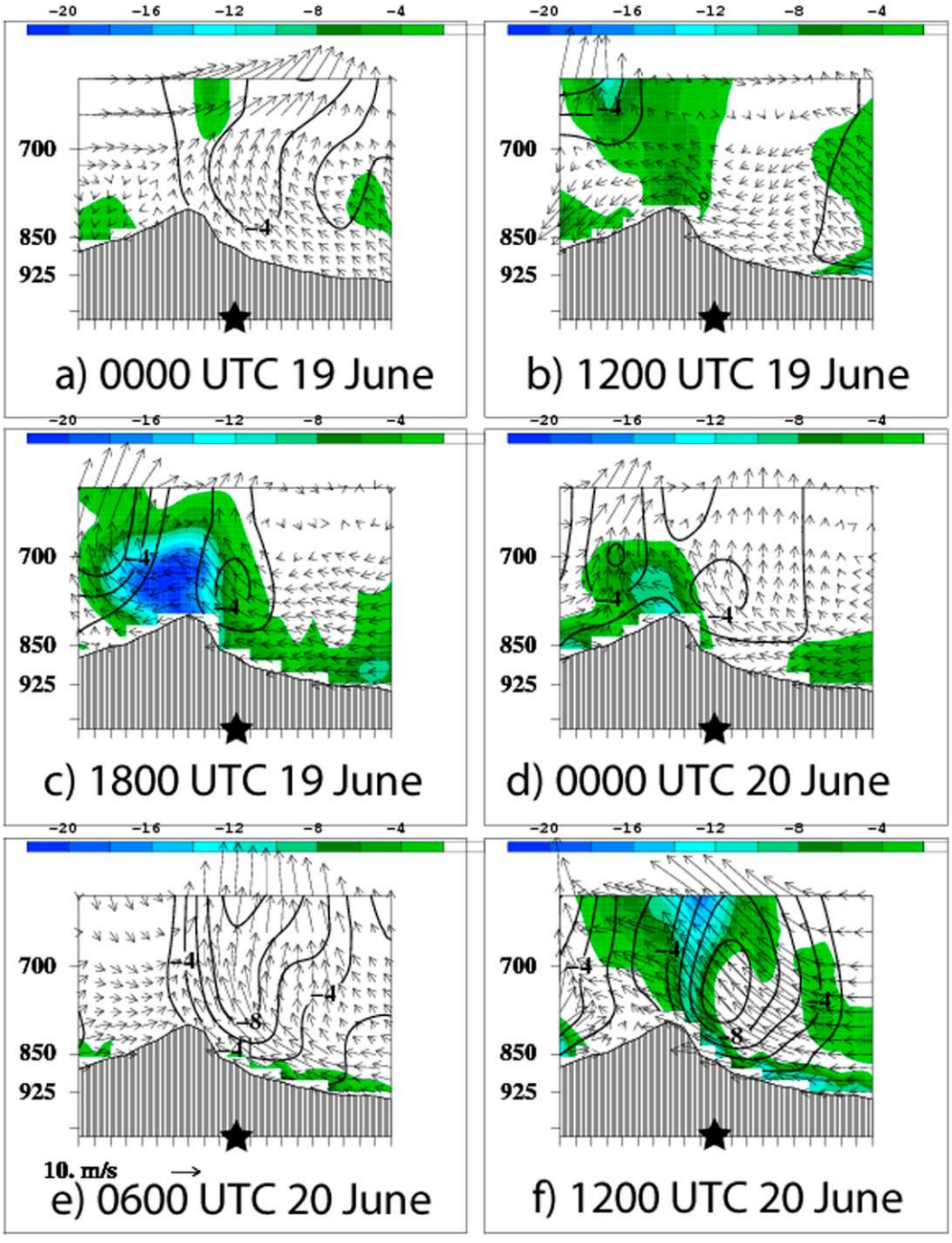

FIG. 11. NARR southwest–northeast cross sections from 48.64°N, 116.52°W to 53.64°N, 111.52°W, with the location of the Calgary International Airport at the halfway point of the cross section and marked with a black star. A blue line identifying the cross-sectional area is in Fig. 9a. Plotted are orographic vertical velocity [ω_{oro}, shaded for ascent, $\times 10^{-3}$ hPa s^{-1} Eq. (10)], vertical velocity (ω, solid contours for ascent, $\times 10^{-3}$ hPa s^{-1}), and circulation vectors (m^2 s^{-1}, gray arrows).

In terms of high-θ_e air location and transport, we observe the following:

- Starting at 0000 UTC 19 June (Fig. 12a), there are two pools of high-θ_e air: one in the southern U.S. plains associated with positive θ_e advection directly from the Gulf of Mexico and another in the northern U.S. plains and southern Canadian prairies. This signature is evident throughout the event, although it is more

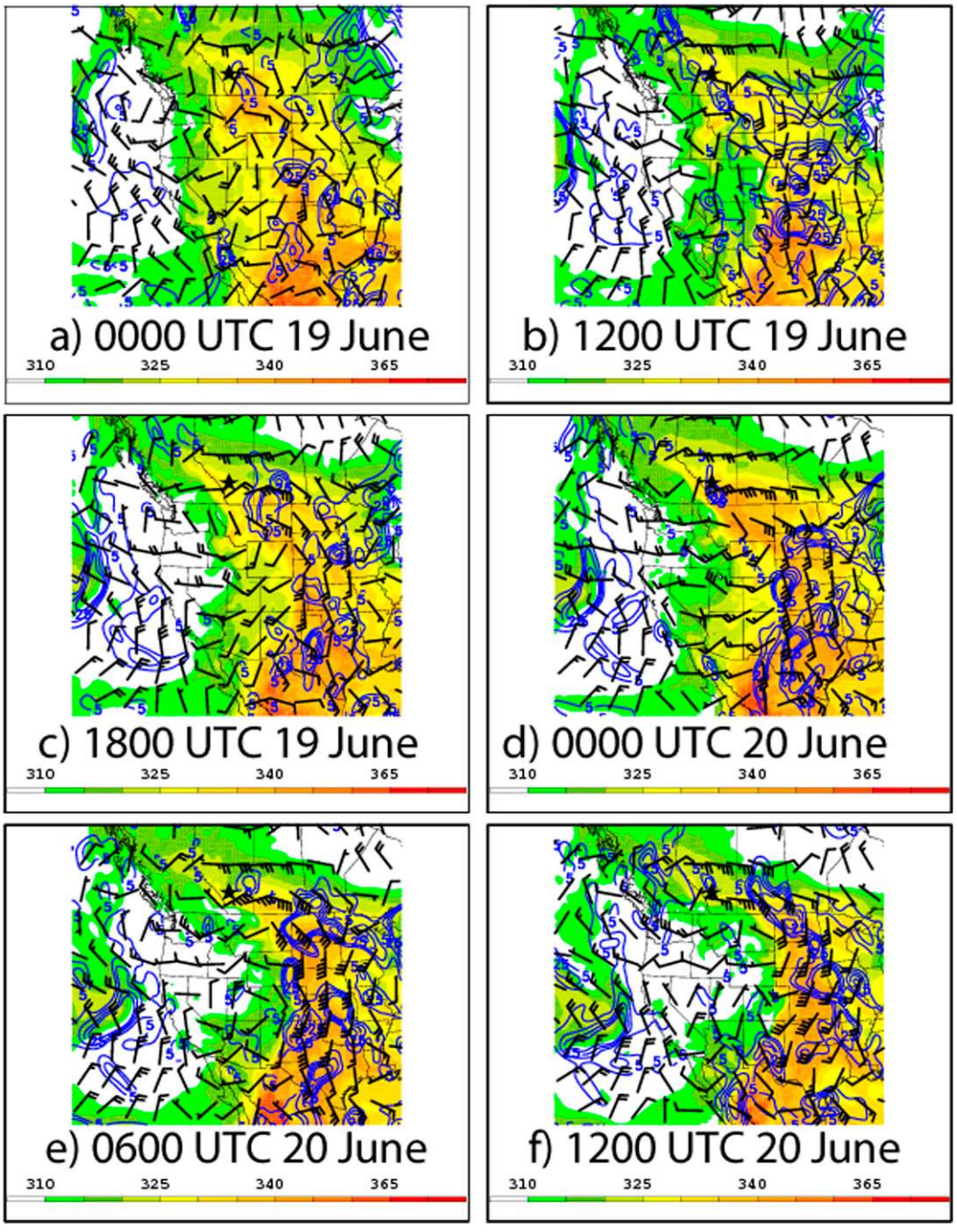

FIG. 12. As in Fig. 9, but for 850-hPa equivalent potential temperature (K, shaded), 850-hPa equivalent potential temperature advection (10^{-5} K s^{-1}, solid blue contours at values of 5, 15, and 25), and winds (kt, where 1 kt = 0.5144 m s^{-1}; barbs). The approximate location of the Calgary International Airport is marked with a black star in each panel.

obvious at certain times (e.g., 0000 UTC 20 June; Fig. 12d) than others (e.g., 1200 UTC 20 June; Fig. 12f).

- Despite the establishment of a strong southerly low-level jet from the Gulf of Mexico to southern Saskatchewan and Alberta starting at 0000 UTC 20 June (Figs. 12d–f), neutral to weak negative θ_e advection is observed between the two pools of high-θ_e air (e.g., over Montana and North Dakota at 0000 UTC 20 June; Fig. 12d). This is strongly suggestive that the positive θ_e ad-

vection into southern Alberta did not trace directly back to the Gulf of Mexico and instead resulted from high-θ_e air pooled in the northern plains.

Previous work on convection in the U.S. Great Plains (e.g., Cheresnick and Basara 2005; Milrad and Kelly 2013) found that air parcel trajectories in such events can originate from within the Great Plains region as opposed to directly from the Gulf of Mexico. The lack of positive θ_e advection between the two pools of high-θ_e air (Fig. 12) suggests that the Gulf of Mexico may not have been a direct moisture source. To address this issue, we performed 5-day (120 h) backward air parcel trajectory runs ending at 700 hPa centered on CYYC every 6 h from 0000 to 1800 UTC 20 June (Fig. 13); results were similar for parcels ending at 850 and 600 hPa. At all four times, no parcel trajectory emanates from the Gulf of Mexico (Fig. 13). In fact, the overwhelming majority of trajectories originate in the Dakotas, Montana, and the southern Canadian prairies. This is especially true at 0600 (Fig. 13b) and 1200 UTC (Fig. 13c), during the heaviest precipitation. As the parcel paths approach southern Alberta, they rapidly ascend within the easterly flow (Fig. 13), further suggestive of orographic ascent.

The idea of "airmass conditioning," or air parcels associated with heavy precipitation events being modified in the U.S. plains was noted by Milrad et al. (2009b, 2010b, 2014a) and Milrad and Kelly (2013) in studies that examined precipitation events in diverse locations (Newfoundland, the U.S. Great Plains, and Quebec). This idea has been widely discussed in the hydrological literature, where it is often referred to as "precipitation recycling" and refers to predominantly longer time scales. Brubaker et al. (1993) stated that continental precipitation can have two moisture sources: 1) advection from external areas (e.g., the Gulf of Mexico) and 2) evapotranspiration from the local land surface. Although numerical estimates vary widely as to how much of the precipitation over the continental United States is due to evapotranspiration from the land surface (Brubaker et al. 1993; Bosilovich and Schubert 2001), many studies (e.g., Dirmeyer and Brubaker 1999; Zangvil et al. 2004; Dominguez and Kumar 2008) have noted that the land surface in the Great Plains is "uniquely vigorous in its land–atmosphere interactions" (Dirmeyer et al. 2009, p. 286), and that these interactions are favored in the warm season (e.g., Brubaker et al. 1993). Cheresnick and Basara (2005) found that for a 2001 Minnesota tornado event, direct moisture advection from the Gulf of Mexico did not have a major effect on airmass modification, while low-level moisture advection from a local source (i.e., evapotranspiration in the Great Plains) did play a large role. More recent work has suggested that at least some of the unique ability of the Great Plains to increase columnar IWV may be due to irrigation (e.g., DeAngelis et al. 2010; Harding and Snyder 2012a,b). Increased IWV may not only alter the moisture source (i.e., Great Plains vs Gulf of Mexico) of heavy precipitation events but also increase the maximum amount of precipitation within a particular event (DeAngelis et al. 2010). Although our results are suggestive of the local land surface playing a role in modifying the air mass (i.e., producing higher θ_e air in the northern U.S. plains) before the Alberta flood, we cannot confirm this assertion without numerical model simulations. These experiments will be a primary component of future work and are discussed further in section 6.

Figure 14 presents IWV [Eq. (5)], IVT vectors [Eq. (6)], and MFC [Eq. (7)]. Figures 14a and 14b show two plumes of large IWV: one in Montana, Saskatchewan, and Alberta, and another in the southern plains emanating from the Gulf of Mexico. Although large (>30 mm) IWV values are located throughout the plains from 1800 UTC 19 June onward (Figs. 14c–f), there are two distinct maxima. For example, at 0000 UTC 20 June (Fig. 14d), the northern maxima of >30 mm is located in southern Saskatchewan, while the southern maxima of >40 mm is located in Texas.

As Ralph et al. (2011), Moore et al. (2012), and Rutz et al. (2014) pointed out, an AR is typically only associated with an extreme precipitation event if MFC occurs; that is, while moisture transport into the affected region is a necessary condition, it is not a sufficient one. This corresponds to Banacos and Schultz's (2005) conclusion that the magnitude of MFC is typically proportional to that of lower-tropospheric mass convergence, implying ascent. MFC can be (but is not solely) caused by orography, when moisture transport vectors intersect elevated terrain, such as the west coast mountain ranges (e.g., Ralph et al. 2004, 2011), or inland mountains (e.g., Brimelow and Reuter 2005; Rutz et al. 2014). In this case, both moisture transport and MFC are observed over the southern Alberta foothills from 1200 UTC 19 June onward (Figs. 14b–f), with MFC maximized over the foothills at 0600 and 1200 UTC 20 June (Figs. 14d,e), during the heaviest precipitation. Our results are consistent with those of Junker et al. (1999), who found that the strongest MFC was found upstream of the initial convection. At 0000 UTC 20 June, when the initial convection is located over the Banff area (Fig. 5a), the strongest MFC is still located to the south near the Alberta–Montana border (Fig. 14d). Finally, Fig. 14 highlights the duration of the event, with strong IVT and MFC observed within the geostrophic easterlies over Calgary and the foothills continuously from 1200 UTC 19 June onward (Figs. 14b–f).

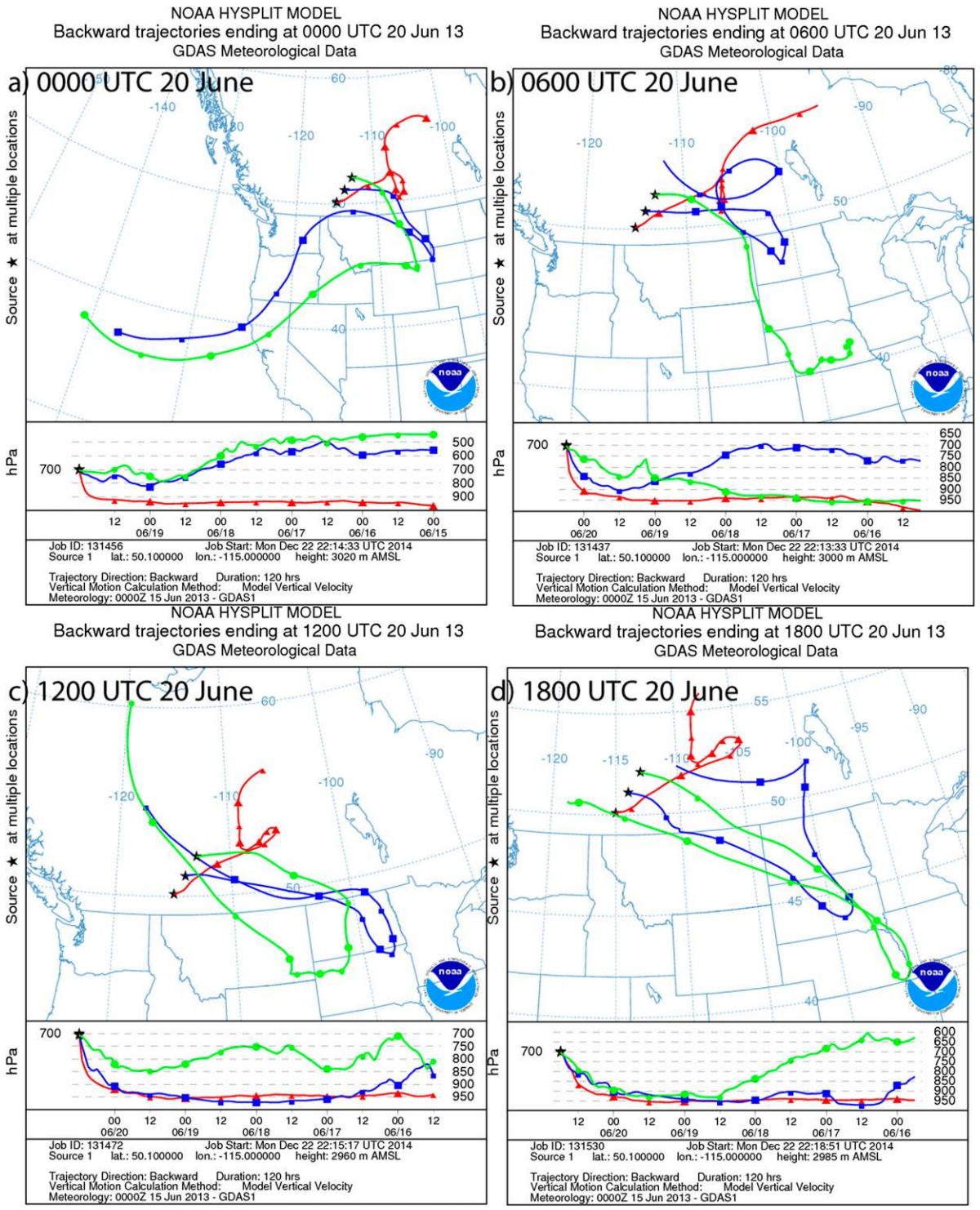

FIG. 13. Three 120-h backward air parcel trajectories from the NOAA HYSPLIT model ending at 700 hPa, and centered on CYYC (from left to right: 50.1°N, 115°W; 51.1°N, 114°W (CYYC); and 52.1°N, 113°W; marked with black stars), for ending times of (a) 0000, (b) 0600, (c) 1200, and (d) 1800 UTC 20 Jun. Note that the map domains are slightly different in each panel.

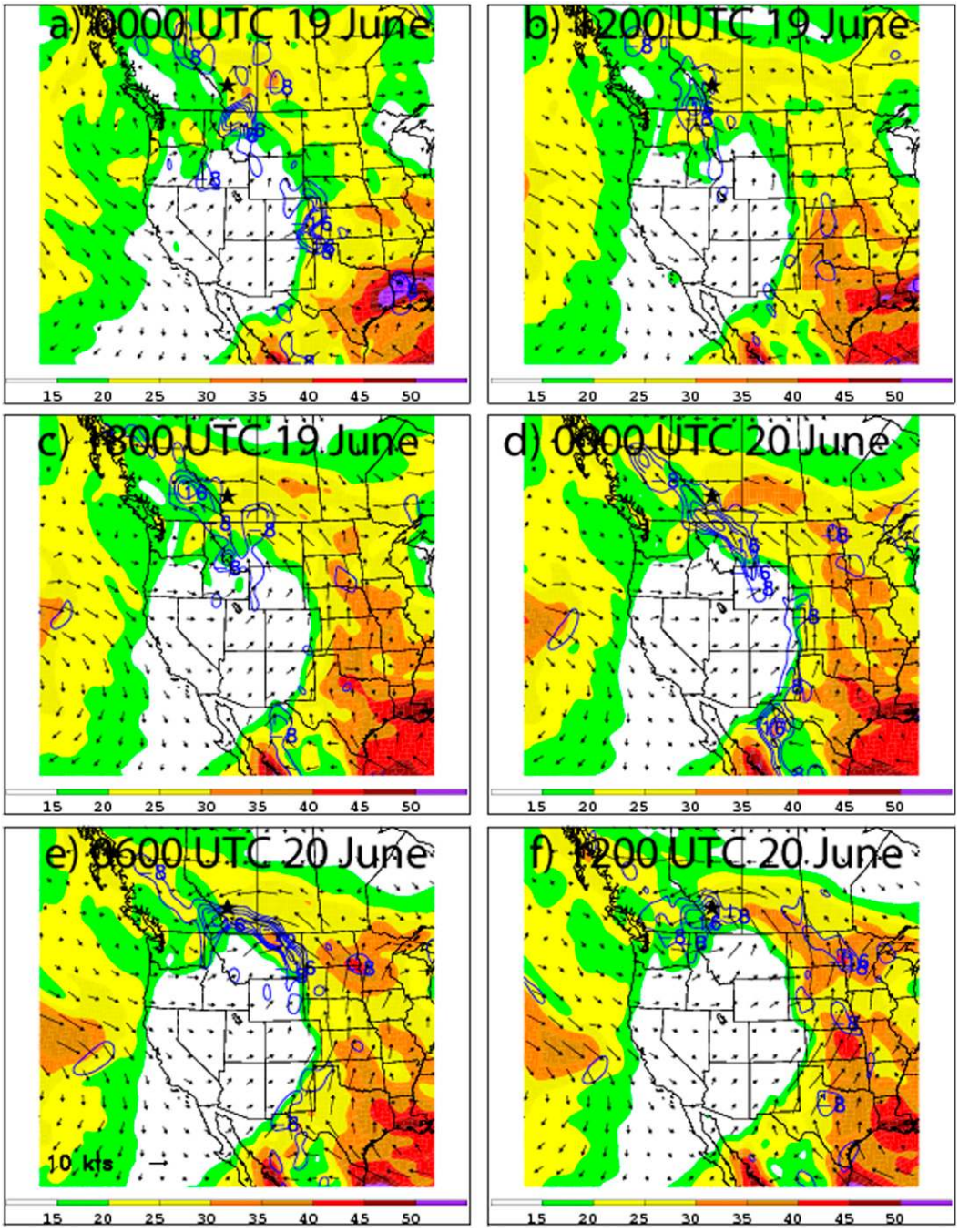

FIG. 14. As in Fig. 9, but for vertically integrated (1000–300 hPa) MFC ($\times 10^{-7}$ kg s^{-1}, blue contours for convergence), 1000–300-hPa IVT (kg m^{-1} s^{-1}, arrows), and IWV (mm, shaded). The approximate location of the Calgary International Airport is marked with a black star in each panel, and a reference IVT vector is shown in the bottom-left panel.

c. *Instability*

To analyze instability, we first define convective (potential) instability (CI):

$$\frac{d\theta_e}{dz} < 0. \tag{8}$$

Second, we define conditional symmetric instability (CSI):

$$\mathrm{MPV}_g^* < 0, \tag{9}$$

where MPV_g^* is the saturated equivalent geostrophic potential vorticity (PVU; 1 PVU = 10^{-6} K kg^{-1} m^2 s^{-1}), explicitly defined by

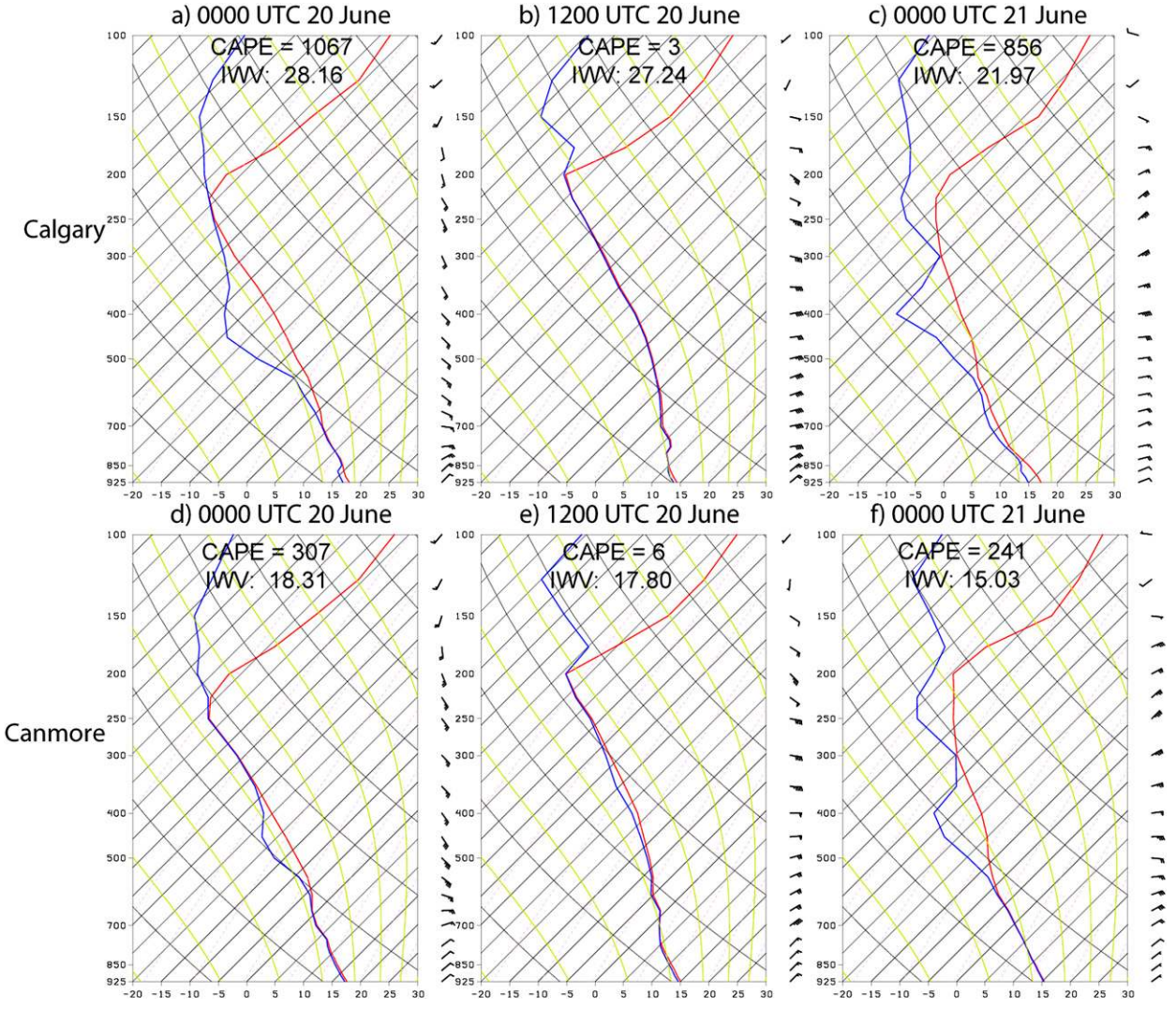

FIG. 15. CFSR soundings for the locations of the (a)–(c) Calgary International Airport and (d)–(f) Canmore at (a),(d) 0000 UTC 20 Jun; (b),(e) 1200 UTC 20 Jun; and (c),(f) 0000 UTC 21 Jun. Temperature and dewpoint (°C) are plotted in red and blue, respectively. Winds (kt, barbs) are plotted on the right-hand side of each panel, and point values of CAPE (J kg^{-1}) and IWV (mm) are written at the top of each panel.

$$\mathrm{MPV}_g^* = g\boldsymbol{\eta}_g \cdot \nabla\theta_e^* , \tag{10}$$

where g is gravity, $\boldsymbol{\eta}_g$ is the three-dimensional geostrophic absolute vorticity vector, ∇ is the gradient operator in x and y, and θ_e^* is the saturated equivalent potential temperature.

Schultz and Schumacher (1999) pointed out that 1) MPV_g^* is not very sensitive to the orientation of a cross section, unlike geostrophic absolute momentum (M_g) surfaces; and that 2) although CI and CSI can coexist and CSI can even precede CI (e.g., Milrad et al. 2014b), CI tends to dominate CSI over time. Bryan and Fritsch (2000) argued for the existence of a sixth stability state in the low and midtroposphere, the moist absolute unstable layer (MAUL), which can be >100 hPa deep and last for >30 min. MAULs often occur in or near MCSs, affecting the structure of the convective region and increasing the degree of saturation in the stratiform region (Bryan and Fritsch 2000). In a case study of convective snow squalls in the Calgary area, Milrad et al. (2014b) found MAULs to be present at times, using both reanalysis datasets and high-resolution numerical simulations.

The nearest radiosonde stations to southern Alberta are in Great Falls, Montana (KTFX), and Edmonton, Alberta (CWSE); given the limited spatial extent of the heaviest rainfall (Fig. 4), we deemed these insufficient to use as proximity soundings. Figure 15 shows CFSR

soundings interpolated to Calgary and Canmore at 0000 UTC 20 June, 1200 UTC 20 June, and 0000 UTC 21 June; we compared the vertical profiles to the NARR and found them to be similar. At 0000 UTC 20 June, Figs. 15a and 15d show conditional instability in both Calgary and Canmore, respectively, although the air is more saturated in Canmore, corresponding to the heavier rainfall at that time (Fig. 5a). Both profiles at 0000 UTC 20 June (Figs. 15a,d) suggest a MAUL (completely saturated, with lapse rates greater than moist adiabatic), particularly in the 850–700-hPa layer, and exhibit moderate CAPE, which is commonly observed in flash flood soundings (e.g., Maddox et al. 1978, 1979, 1980; Gochis et al. 2015). By 1200 UTC 20 June (Figs. 15b,e), both the Calgary and Canmore profiles are essentially moist neutral, indicative of strong moist-adiabatic ascent (e.g., Gyakum 2008) and essentially no CAPE. Finally, at 0000 UTC 21 June (Figs. 15c,f), the Calgary profile has become slightly less saturated, while conditional instability (moderate CAPE) and a MAUL (again, in the 850–700-hPa layer) are still evident at Canmore. The veering wind profiles at both locations suggest lower- and mid-tropospheric WAA at 0000 UTC 20 June (Figs. 15a,d), which weakens at later times (Figs. 15b,c,e,f); these observations are consistent with our MSLP diagnostics (Figs. 10b,e,h).

Using the same cross-sectional area as in Fig. 11, Fig. 16 investigates CI and CSI in the flood region from 0000 UTC 19 June to 1200 UTC 20 June. The cross section is perpendicular to both the terrain and the thermal wind (Schultz and Schumacher 1999). At 0000 UTC 19 June, Fig. 16a shows a large region of CSI near Calgary, collocated with weak CI. However, by 1800 UTC 19 June (Fig. 16d), CSI decreases and CI markedly increases, evidenced by the tightly spaced isentropes in the lowest 150 hPa. The same signature is seen over both Calgary and the foothills at 0000 and 0600 UTC 20 June (Figs. 16d,e), with CI located from the surface to around 700 hPa at 0000 UTC and from the surface to approximately 650 hPa at 0600 UTC. The CI signature weakens slightly by 1200 UTC (Fig. 16f). Additionally, given the large magnitude of the lower-tropospheric CI from 1800 UTC 19 June to 0600 UTC 20 June (Figs. 16c–e), the CI likely acted to further destabilize the atmosphere (increase lapse rates), leading to and maintaining the conditionally unstable/MAUL signatures seen in Figs. 15a and 15d. This would also explain why as the CI weakens in the 0600–1200 UTC 20 June time period (Figs. 16d,e), the vertical profiles at Calgary and Canmore transition from conditionally unstable at 0000 UTC (Figs. 15a,d) to moist neutral at 1200 UTC 20 June (Figs. 15b,e)

Because of the relatively coarse grid spacing of any reanalysis, some of the instability structures discussed above may not be completely resolved. As in Milrad et al. (2014b), we plan to address these issues with convection-permitting high-resolution numerical simulations in future work (detailed in section 6b).

6. Conclusions

a. Discussion

The June 2013 Alberta flood was the costliest natural disaster in Canadian history, resulting in nearly CAD $6 billion in damage. A myriad of meteorological and hydrological factors played a role in the severity of the event, including an above-normal melting snowpack and antecedent spring rainfall that saturated the soil prior to the extreme rainfall event of 19–21 June. Here, we focused primarily on a meteorological analysis of the extreme rainfall event, which featured a complex multiscale evolution and exhibited many synoptic-scale similarities to blocking flow patterns during the 2013 Great Colorado flood and other infamous Front Range flash floods (e.g., Maddox et al. 1978; Gochis et al. 2015).

The antecedent planetary- and synoptic-scale evolution started in the western North Pacific on 11 June, when baroclinic development occurring in East Asia led to downstream Rossby wave train development and an amplified flow pattern across the North Pacific (Figs. 6, 7). Five days before event onset (0000 UTC 15 June), a strong pressure gradient between a cyclone in the Aleutian Islands and a 1032-hPa subtropical anticyclone (Figs. 6c, 8c) contributed to a strong southerly AR (IWV $>$ 40 mm) into Alaska (Figs. 8c,d). Subsequently, a strong ridge over Alaska and a cyclonic DT disturbance just off the British Columbia coast formed a Rex block over the northeastern North Pacific (Fig. 6d). The Rex block broke down when a cyclonic DT disturbance acted to ''kick'' the initial cyclonic DT disturbance into British Columbia and Washington, leading to lee MSLP cyclogenesis in Montana and the establishment of persistent easterly upslope flow into southern Alberta by 0000 UTC 19 June (Fig. 9).

We used an ingredients-based approach (lift, moisture, and instability) for heavy precipitation. Although $\mathbf{Q}_n$ convergence (frontogenesis) was evident at the start of the event (Fig. 10b), the times of heaviest precipitation (0600 and 1200 UTC 20 June) were characterized by $\mathbf{Q}_s$ convergence (Figs. 10d,g), primarily associated with strong WAA. Figure 11 showed that orographic ascent likely helped to enhance and prolong precipitation, especially later in the event (e.g., 1200 UTC 20 June), working in concert with the QG ascent-forcing processes (primarily WAA). In future work, we will aim to quantify the contributions of the local orography to ascent and precipitation amounts, using terrain-removal sensitivity experiments in high-resolution numerical simulations.

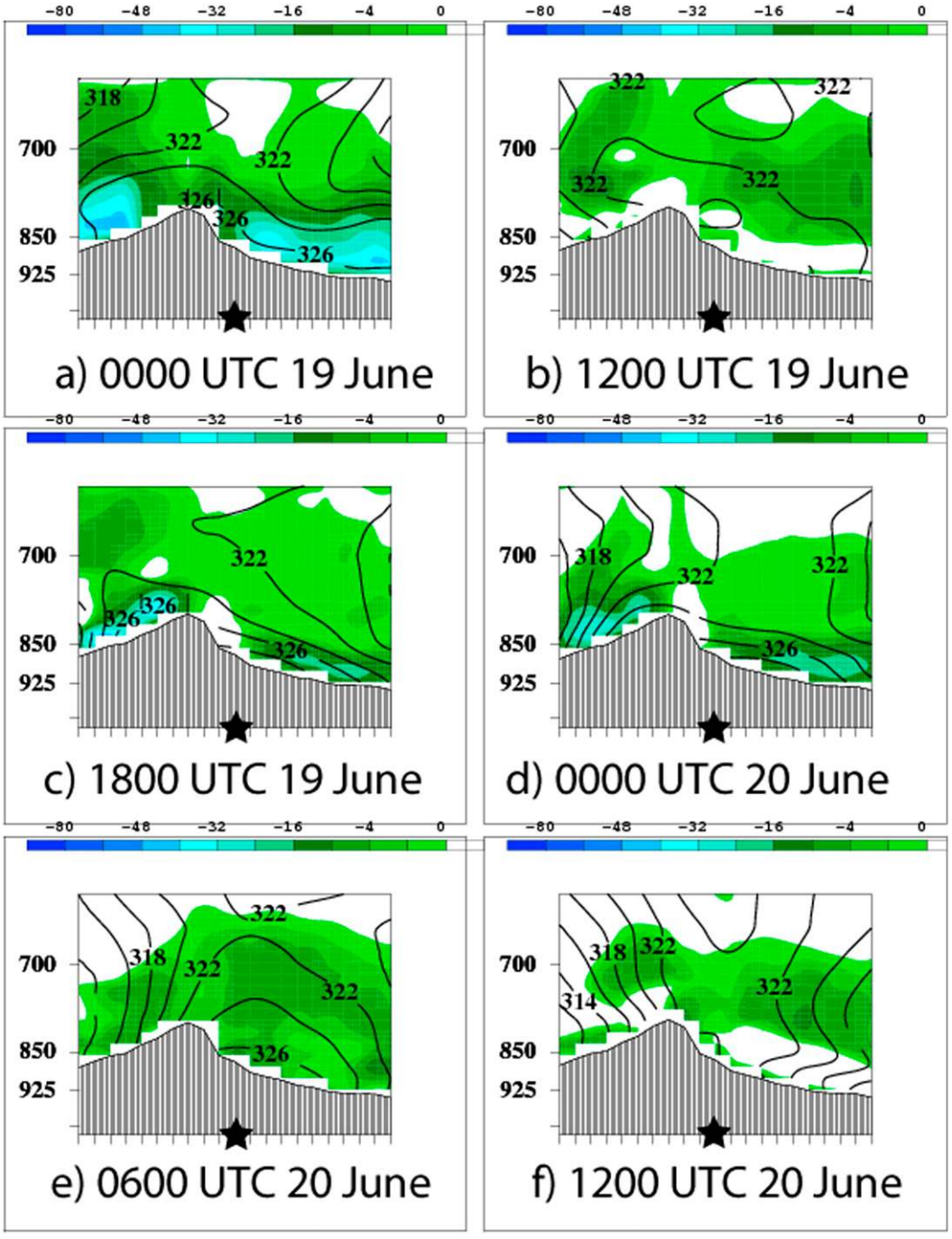

FIG. 16. As in Fig. 11, but for saturated equivalent geostrophic potential vorticity ($\times 10^{-7}$ m^2 s^{-1} K kg^{-1}, shaded for negative values) and equivalent potential temperature (K, solid contours).

Moisture transport and more importantly, MFC, were evident just prior to and during the precipitation period both over Calgary and the foothills (Fig. 14). As Junker et al. (1999) found, MFC was located upstream of the initial convective cells (Fig. 14d), which combined with positive θ_e advection led to backbuilding of new convective echoes to the southeast (e.g., Maddox et al. 1978; Schumacher and Johnson 2005). Two pools of high-θ_e air were present throughout the event: one in the northern U.S. plains and one closer to the Gulf of Mexico (Fig. 12). Air parcels originated mostly from the high-θ_e air pool in the northern U.S. plains (Figs. 12, 13),

and not a single air parcel trajectory originated from the Gulf of Mexico (Fig. 13). This questions the importance of the Great Plains's southerly low-level jet for this event; that is, despite the lack of a direct connection to the Gulf of Mexico, it is unclear how much of the high-θ_e air in the northern plains originated from the Gulf of Mexico at an earlier time and how much was created in situ due to evapotranspiration from the land surface (i.e., precipitation recycling).

QG and orographic ascent acted to release conditional instability in a moderate CAPE environment during the first part of the event (0000–0600 UTC 20 June), before a transition to moist-neutral stability by 1200 UTC (Fig. 15). The release of CI further acted to steepen lower-tropospheric lapse rates (Fig. 15) and sustain conditional instability, such that it could continue to be released by rising air. Conditional instability and MAULs were more prevalent throughout the event (0000 UTC 20 June–0000 UTC 21 June; Fig. 15) in the foothills (i.e., Canmore) than in Calgary, coinciding with higher precipitation amounts (Table 1).

b. *Future work*

There are multiple avenues of future work on this case. The first endeavor will be to perform nested-grid high-resolution model simulations, including using a convection-permitting inner domain (e.g., 3-km grid spacing). With the model simulations, we will be able to do the following:

- Evaluate the ability of the model to accurately reproduce the magnitude and location of the precipitation.
- Gain further insight into the physical mechanisms responsible for the heavy precipitation.
  - With respect to ascent, we will use a simple terrain-reduction scheme (e.g., Flesch and Reuter 2012) to evaluate the impact of the orography on ascent and precipitation amounts.
  - With respect to instability, one outstanding question is how realistic the MAULs observed in the reanalysis datasets are and whether they are in fact caused and/or sustained by strong lower-tropospheric CI during the early part of the event.
- Gain further insight into the role of antecedent rainfall (soil moisture) and the local land surface (i.e., precipitation recycling).
- Compare and contrast the results to operational numerical model forecasts. Quantitative precipitation forecasts remain less skillful than mass field forecasts (e.g., Gyakum 2008; Milrad et al. 2014a), and our simulations will help assess if the underestimation of the heaviest precipitation was due to certain physical parameterizations, poor forecasts of necessary meteorological ingredients, or a combination of both.

Other future work could involve a quantification of various antecedent large-scale flow features. While Pfahl and Wernli (2012) quantified the importance of cyclones in extreme precipitation events, little work has explicitly quantified the importance or necessity of downstream anticyclones. These avenues of research would likely necessitate potential vorticity inversion techniques.

Acknowledgments. This research was supported by an internal research grant from Embry-Riddle Aeronautical University and by grants from the Natural Sciences and Engineering Research Council of Canada (Discovery, and Climate Change and Atmospheric Research Grants). Thanks to NOAA and Environment Canada for access to climate, radar, and reanalysis data. The authors would also like to thank the three anonymous reviewers for their constructive comments toward revising this manuscript.

REFERENCES

Alberta Environment, 2013: Alberta's river basins, river flows and levels. Subset used: April-August 2013, accessed August 2013. [Available online at http://www.environment.alberta.ca/apps/basins/.]

Archambault, H. M., L. F. Bosart, D. Keyser, and J. M. Cordeira, 2013: A climatological analysis of the extratropical flow response to recurving western North Pacific tropical cyclones. *Mon. Wea. Rev.,* **141,** 2325–2346, doi:10.1175/MWR-D-12-00257.1.

Banacos, P. C., and D. M. Schultz, 2005: The use of moisture flux convergence in forecasting convective initiation: Historical and operational perspectives. *Wea. Forecasting,* **20,** 351–366, doi:10.1175/WAF858.1.

Bosilovich, M. G., and S. D. Schubert, 2001: Precipitation recycling over the central United States diagnosed from the GEOS-1 data assimilation system. *J. Hydrometeor.,* **2,** 26–35, doi:10.1175/1525-7541(2001)002<0026:PROTCU>2.0.CO;2.

Brimelow, J. C., and G. W. Reuter, 2005: Transport of atmospheric moisture during three extreme rainfall events over the Mackenzie River basin. *J. Hydrometeor.,* **6,** 423–440, doi:10.1175/JHM430.1.

Brubaker, K. L., D. Enekhabi, and P. S. Eagleson, 1993: Estimation of continental precipitation recycling. *J. Climate,* **6,** 1077–1089, doi:10.1175/1520-0442(1993)006<1077:EOCPR>2.0.CO;2.

Bryan, G. H., and J. M. Fritsch, 2000: Moist absolute instability: The sixth static stability state. *Bull. Amer. Meteor. Soc.,* **81,** 1207–1230, doi:10.1175/1520-0477(2000)081<1287:MAITSS>2.3.CO;2.

Calgary Herald, 2014: Herald wins Online Journalism Award for flood coverage. [Available online at http://calgaryherald.com/news/local-news/herald-wins-online-journalism-award-for-flood-coverage.]

Caracena, F., R. A. Maddox, L. R. Hoxit, and C. F. Chappell, 1979: Mesoanalysis of the Big Thompson storm. *Mon. Wea. Rev.,* **107,** 1–17, doi:10.1175/1520-0493(1979)107<0001:MOTBTS>2.0.CO;2.

Cheresnick, D. R., and J. B. Basara, 2005: The impact of land–atmosphere interactions on the Benson, Minnesota, tornado of 11 June 2001. *Bull. Amer. Meteor. Soc.,* **86,** 637–642, doi:10.1175/BAMS-86-5-637.

Climat-Quebec, 2014: Data access, data and climate networks. Accessed June 2014. [Available online at http://www.climat-quebec.qc.ca/home.php?id=guic_d_donn&mpn=misc.]

DeAngelis, A., F. Dominguez, Y. Fan, A. Robock, M. D. Kustu, and D. Robinson, 2010: Evidence of enhanced precipitation due to irrigation over the Great Plains of the United States. *J. Geophys. Res.,* **115,** D15115, doi:10.1029/2010JD013892.

Dirmeyer, P. A., and K. L. Brubaker, 1999: Contrasting evaporative moisture sources during the drought of 1988 and the flood of 1993. *J. Geophys. Res.,* **104,** 19 383–19 397, doi:10.1029/1999JD900222.

——, and J. L. Kinter III, 2010: Floods over the U.S. Midwest: A regional water cycle perspective. *J. Hydrometeor.,* **11,** 1172–1181, doi:10.1175/2010JHM1196.1.

——, C. A. Schlosser, and K. L. Brubaker, 2009: Precipitation, recycling, and land memory: An integrated analysis. *J. Hydrometeor.,* **10,** 278–288, doi:10.1175/2008JHM1016.1.

Dominguez, F., and P. Kumar, 2008: Precipitation recycling variability and ecoclimatological stability—A study using NARR data. Part I: Central U.S. plains ecoregion. *J. Climate,* **21,** 5165–5186, doi:10.1175/2008JCLI1756.1.

Doswell, C. A., III, H. E. Brooks, and R. A. Maddox, 1996: Flash flood forecasting: An ingredients-based methodology. *Wea. Forecasting,* **11,** 560–581, doi:10.1175/1520-0434(1996)011<0560:FFFAIB>2.0.CO;2.

Draxler, R. R., and G. D. Rolph, 2012: HYSPLIT—Hybrid Single Particle Lagrangian Integrated Trajectory model. [Available online at http://ready.arl.noaa.gov/HYSPLIT.php.]

Environment Canada, 2014a: About radar. [Available online at http://www.ec.gc.ca/meteo-weather/default.asp?lang=En&n=2B931828-1.]

——, 2014b: Canada's top ten weather stories for 2013. [Available online at http://www.ec.gc.ca/meteo-weather/default.asp?lang=En&n=5BA5EAFC-1.]

——, 2014c: Canadian historical weather radar. Subset used: 19-21 June 2013, accessed June 2014. [Available online at http://climate.weather.gc.ca/radar/index_e.html.]

——, 2014d: Canadian historical climate data. Accessed June 2014. [Available online at http://climate.weather.gc.ca/.]

Flesch, T. K., and G. W. Reuter, 2012: WRF model simulation of two Alberta flooding events and the impact of topography. *J. Hydrometeor.,* **13,** 695–708, doi:10.1175/JHM-D-11-035.1.

Gochis, D., and Coauthors, 2015: The Great Colorado Flood of September 2013. *Bull. Amer. Meteor. Soc.,* in press.

Government of Alberta, 2014: Alberta 2013–2014 flood recovery update. [Available online at http://alberta.ca/Flood-recovery-update.cfm.]

Gyakum, J. R., 2008: The application of Fred Sanders' teaching to current research on extreme cold-season precipitation events in the Saint Lawrence River Valley region. *Synoptic–Dynamic Meteorology and Weather Analysis and Forecasting: A Tribute to Fred Sanders, Meteor. Monogr.,* No. 55, Amer. Meteor. Soc., 241–250.

——, and P. J. Roebber, 2001: The 1998 ice storm—Analysis of a planetary-scale event. *Mon. Wea. Rev.,* **129,** 2983–2997, doi:10.1175/1520-0493(2001)129<2983:TISAOA>2.0.CO;2.

Hamill, T. M., 2014: Performance of operational model precipitation forecast guidance during the 2013 Colorado Front-Range floods. *Mon. Wea. Rev.,* **142,** 2609–2618, doi:10.1175/MWR-D-14-00007.1.

Harding, K. J., and P. K. Snyder, 2012a: Modeling the atmospheric response to irrigation in the Great Plains. Part I: General impacts on precipitation and the energy budget. *J. Hydrometeor.,* **13,** 1667–1686, doi:10.1175/JHM-D-11-098.1.

——, and ——, 2012b: Modeling the atmospheric response to irrigation in the Great Plains. Part II: The precipitation of irrigated water and changes in precipitation recycling. *J. Hydrometeor.,* **13,** 1667–1686, doi:10.1175/JHM-D-11-098.1.

Hoskins, B. J., I. Draghici, and H. C. Davies, 1978: A new look at the omega equation. *Quart. J. Roy. Meteor. Soc.,* **104,** 31–38, doi:10.1002/qj.49710443903.

Huffington Post Alberta, 2014: 19 most powerful images from the Alberta floods. [Available online at http://www.huffingtonpost.ca/2014/06/17/alberta-flood-photos_n_5504373.html.]

Junker, N. W., R. S. Schneider, and S. L. Fauver, 1999: A study of heavy rainfall events during the Great Midwest Flood of 1993. *Wea. Forecasting,* **14,** 701–712, doi:10.1175/1520-0434(1999)014<0701:ASOHRE>2.0.CO;2.

Kalnay, E., and Coauthors, 1996: The NCEP/NCAR 40-Year Reanalysis Project. *Bull. Amer. Meteor. Soc.,* **77,** 437–471, doi:10.1175/1520-0477(1996)077<0437:TNYRP>2.0.CO;2.

Kanamitsu, M., 1989: Description of the NMC global data assimilation scheme. *Wea. Forecasting,* **4,** 335–342, doi:10.1175/1520-0434(1989)004<0335:DOTNGD>2.0.CO;2.

Keyser, D., M. J. Reeder, and R. J. Reed, 1988: A generalization of Petterssen's frontogenesis function and its relation to the forcing of vertical motion. *Mon. Wea. Rev.,* **116,** 762–780, doi:10.1175/1520-0493(1988)116<0762:AGOPFF>2.0.CO;2.

——, B. D. Schmidt, and D. G. Duffy, 1992: Quasigeostrophic vertical motions diagnosed from along- and cross-isentrope components of the **Q** vector. *Mon. Wea. Rev.,* **120,** 731–741, doi:10.1175/1520-0493(1992)120<0731:QVMDFA>2.0.CO;2.

Koch, S., M. DesJardins, and P. Kocin, 1983: An interactive Barnes objective map analysis scheme for use with satellite and conventional data. *J. Climate Appl. Meteor.,* **22,** 1487–1503, doi:10.1175/1520-0450(1983)022<1487:AIBOMA>2.0.CO;2.

Lackmann, G. M., and J. R. Gyakum, 1996: The synoptic- and planetary-scale signatures over the Mackenzie River Basin. *Atmos.–Ocean,* **34,** 647–674, doi:10.1080/07055900.1996.9649581.

Lavers, D. A., and G. Villarini, 2013: Were global numerical weather prediction systems capable of forecasting the extreme Colorado rainfall of 9–16 September 2013? *Geophys. Res. Lett.,* **40,** 6405–6410, doi:10.1002/2013GL058282.

Lynch, S. L., and R. S. Schumacher, 2014: Ensemble-based analysis of the May 2010 extreme rainfall in Tennessee and Kentucky. *Mon. Wea. Rev.,* **142,** 222–239, doi:10.1175/MWR-D-13-00020.1.

Maddox, R. A., L. R. Hoxit, C. F. Chappell, and F. Caracena, 1978: Comparison of meteorological aspects of the Big Thompson and Rapid City flash floods. *Mon. Wea. Rev.,* **106,** 375–389, doi:10.1175/1520-0493(1978)106<0375:COMAOT>2.0.CO;2.

——, C. F. Chappell, and L. R. Hoxit, 1979: Synoptic and meso-α aspects of flash flood events. *Bull. Amer. Meteor. Soc.,* **60,** 115–123, doi:10.1175/1520-0477-60.2.115.

——, F. Canova, and L. R. Hoxit, 1980: Meteorological characteristics of flash flood events over the western United States. *Mon. Wea. Rev.,* **108,** 1866–1877, doi:10.1175/1520-0493(1980)108<1866:MCOFFE>2.0.CO;2.

Mahfouf, J. F., B. Brasnett, and S. Gagnon, 2007: A Canadian precipitation analysis (CaPA) project: Description and preliminary results. *Atmos.–Ocean,* **45,** 1–17, doi:10.3137/ao.450101.

Martin, J. E., 1999: Quasigeostrophic forcing of ascent in the occluded sector of cyclones and the trowal airstream. *Mon. Wea. Rev.,* **127,** 70–88, doi:10.1175/1520-0493(1999)127<0070:QFOAIT>2.0.CO;2.

——, 2006a: *Mid-latitude Atmospheric Dynamics: A First Course.* John Wiley and Sons Ltd., 324 pp.

——, 2006b: The role of shearwise and transverse quasigeostrophic vertical motions in the midlatitude cyclone life cycle. *Mon. Wea. Rev.,* **134,** 1174–1193, doi:10.1175/MWR3114.1.

Mesinger, F., and Coauthors, 2006: North American Regional Reanalysis. *Bull. Amer. Meteor. Soc.,* **87,** 343–360, doi:10.1175/BAMS-87-3-343.

Milbrandt, J. A., and M. K. Yau, 2001: A mesoscale modeling study of the 1996 Saguenay Flood. *Mon. Wea. Rev.,* **129,** 1419–1440, doi:10.1175/1520-0493(2001)129<1419:AMMSOT>2.0.CO;2.

Milrad, S. M., and C. M. Kelly, 2013: Synoptic-scale precursors, characteristics, and typing of nocturnal mesoscale convective complexes in the Great Plains. *Electron. J. Severe Storms Meteor.,* **8** (4). [Available online at http://www.ejssm.org/ojs/index.php/ejssm/issue/view/46.]

——, E. H. Atallah, and J. R. Gyakum, 2009a: Dynamical and precipitation structures of poleward-moving tropical cyclones in eastern Canada, 1979–2005. *Mon. Wea. Rev.,* **137,** 836–851, doi:10.1175/2008MWR2578.1.

——, ——, and ——, 2009b: Synoptic-scale characteristics and precursors of cool-season precipitation events at St John's, Newfoundland, 1979–2005. *Wea. Forecasting,* **24,** 667–689, doi:10.1175/2008WAF2222167.1.

——, ——, and ——, 2010a: A diagnostic examination of consecutive extreme cool-season precipitation events at St. John's, Newfoundland, in December 2008. *Wea. Forecasting,* **25,** 997–1026, doi:10.1175/2010WAF2222371.1.

——, ——, and ——, 2010b: Synoptic typing of extreme cool-season precipitation events at St. John's, Newfoundland, 1979–2005. *Wea. Forecasting,* **25,** 562–586, doi:10.1175/2009WAF2222301.1.

——, ——, ——, and G. Dookhie, 2014a: Synoptic-scale precursors and typing of warm-season precipitation events at Montreal, Quebec. *Wea. Forecasting,* **29,** 419–444, doi:10.1175/WAF-D-13-00030.1.

——, J. R. Gyakum, K. Lombardo, and E. H. Atallah, 2014b: On the dynamics, thermodynamics, and forecast model evaluation of two snow-burst events in southern Alberta. *Wea. Forecasting,* **29,** 725–749, doi:10.1175/WAF-D-13-00099.1.

Moore, B. J., P. J. Neiman, F. M. Ralph, and F. E. Barthold, 2012: Physical processes associated with heavy flooding rainfall in Nashville, Tennessee, and vicinity during 1–2 May 2010: The role of an atmospheric river and mesoscale convective systems. *Mon. Wea. Rev.,* **140,** 358–378, doi:10.1175/MWR-D-11-00126.1.

Newman, M., G. N. Kiladis, K. M. Weickmann, F. M. Ralph, and P. D. Sardeshmukh, 2012: Relative contributions of synoptic and low-frequency eddies to time-mean atmospheric moisture transport, including the role of atmospheric rivers. *J. Climate,* **25,** 7341–7361, doi:10.1175/JCLI-D-11-00665.1.

Pfahl, S., and H. Wernli, 2012: Quantifying the relevance of cyclones for precipitation extremes. *J. Climate,* **25,** 6770–6780, doi:10.1175/JCLI-D-11-00705.1.

Ralph, F. M., P. J. Neiman, and G. A. Wick, 2004: Satellite and CALJET aircraft observations of atmospheric rivers over the eastern North Pacific Ocean during the winter of 1997/98. *Mon. Wea. Rev.,* **132,** 1721–1745, doi:10.1175/1520-0493(2004)132<1721:SACAOO>2.0.CO;2.

——, ——, G. N. Kiladis, K. Weickmann, and D. W. Reynolds, 2011: A multiscale observational case study of a North Pacific atmospheric river exhibiting tropical–extratropical connections and a mesoscale frontal wave. *Mon. Wea. Rev.,* **139,** 1169–1189, doi:10.1175/2010MWR3596.1.

Rex, D. F., 1950: Blocking action in the middle troposphere and its effect upon regional climate. Part I: An aerological study of blocking action. *Tellus,* **2A,** 196–211, doi:10.1111/j.2153-3490.1950.tb00331.x.

Roberge, A., J. Gyakum, and E. Atallah, 2009: Analysis of intense poleward water vapor transports into high latitudes of western North America. *Wea. Forecasting,* **24,** 1732–1747, doi:10.1175/2009WAF2222198.1.

Rutz, J. J., W. J. Steenburgh, and F. M. Ralph, 2014: Climatological characteristics of atmospheric rivers and their inland penetration over the western United States. *Mon. Wea. Rev.,* **142,** 905–921, doi:10.1175/MWR-D-13-00168.1.

Saha, S., and Coauthors, 2010: The NCEP Climate Forecast System Reanalysis. *Bull. Amer. Meteor. Soc.,* **91,** 1015–1057, doi:10.1175/2010BAMS3001.1.

Schultz, D. M., and P. N. Schumacher, 1999: The use and misuse of conditional symmetric instability. *Mon. Wea. Rev.,* **127,** 2709–2732, doi:10.1175/1520-0493(1999)127<2709:TUAMOC>2.0.CO;2.

Schumacher, R. S., and R. H. Johnson, 2005: Organization and environmental properties of extreme-rain-producing mesoscale convective systems. *Mon. Wea. Rev.,* **133,** 961–976, doi:10.1175/MWR2899.1.

——, and ——, 2006: Characteristics of U.S. extreme rain events during 1999–2003. *Wea. Forecasting,* **21,** 69–85, doi:10.1175/WAF900.1.

——, and ——, 2008: Mesoscale processes contributing to extreme rainfall in a midlatitude warm-season flash flood. *Mon. Wea. Rev.,* **136,** 3964–3986, doi:10.1175/2008MWR2471.1.

——, and ——, 2009: Quasi-stationary, extreme-rain-producing convective systems associated with midlevel cyclonic circulations. *Wea. Forecasting,* **24,** 555–574, doi:10.1175/2008WAF2222173.1.

Szeto, K., W. Henson, R. Stewart, and G. Gascon, 2011: The catastrophic June 2002 prairie rainstorm. *Atmos.–Ocean,* **49,** 380–395, doi:10.1080/07055900.2011.623079.

Zangvil, A., D. H. Portis, and P. J. Lamb, 2004: Investigation of the large-scale atmospheric moisture field over the midwestern United States in relation to summer precipitation. Part II: Recycling of local evapotranspiration and association with soil moisture and crop yields. *J. Climate,* **17,** 3283–3301, doi:10.1175/1520-0442(2004)017<3283:IOTLAM>2.0.CO;2.